ABSTRACT

Title of dissertation: MICROWAVE EMISSION AND ELECTRON TEMPERATURE IN THE MARYLAND CENTRIFUGAL EXPERIMENT

Remington R. Reid, Doctor of Philosophy, 2013

Dissertation directed by: Professor Richard Ellis
Department of Physics

The use of two magnetised plasma waves as electron temperature diagnostics for the Maryland centrifugal ecperiment (MCX) are explored. First, microwave emission in the whistler mode is examined and ultimately found to be a poor candidate for diagnostic purposes owing to reflections from elsewhere in the plasma confusing the signal. Second, the electron Bernstein wave is found to offer promise as means to measure the radial electron temperature profile. Several numeric codes are developed to analyze the observed microwave emission and calculate the electron temperature profile. Measurements of electron Bernstein wave emission indicate that the electrons in the plasma attain temperatures close to 100 eV. Clear evidence is shown that the measurements are not influenced by reflections or emission from hot ($T_e > 1$keV) superthermal electrons. The measured electron temperature is shown to be in reasonable agreement with recent measurements of the plasma ion temperature.

Microwave Emission and Electron Temperature in the Maryland Centrifugal Experiment.

by

Remington R. Reid

Dissertation submitted to the Faculty of the Graduate School of the
University of Maryland, College Park in partial fulfillment
of the requirements for the degree of
Doctor of Philosophy
2013

Advisory Committee:
Professor Richard F. Ellis
Professor Adil B. Hassam
Dr. John C. Rodgers
Professor Douglas C. Hamilton
Professor Victor L. Granatstein

Dedication

To my parents. Without them, where would I be?

Acknowledgments

There is a long list of people to thank helping me complete this work. This is true for every thesis, but doubly so when the funding for your experiment dries up halfway through your work! Many of these people have not only been outstanding colleagues but also friends, making IREAP a wonderful home these last six years. Dr. Ellis, my advisor, who gave me the opportunity to do this research and somehow found funds to keep me working though the completion of my thesis. Dr. William Young, who's time as a graduate student on MCX overlapped most of mine, taught me how to run MCX, assisted late into the night taking data and made MCX a great place to work. Dr. Carlos Romero-Talamás, who has truly been a bottomless source of support, advice and encouragement throughout. Dr. Adil Hassam, who taught me plasma physics and was always willing to talk about any aspect of the field. Dr. John Rodgers lent me essentially all of the microwave hardware, who also taught me everything I know about microwaves and high voltage systems. Christina Allen, who first demonstrated microwave emission from MCX as a summer student. Jay Pyle and Don Martin who not only assisted in the manufacture of mission critical hardware but also lent me their wisdom and humor. Brian Quinn who treated my facilities problems like they were his own. Dr. Tim Koeth who lent me a truly excellent X-ray camera, and Dr. Howard Milchberg for lending the metal filters needed to make it work. Last but most of all, my wife Jennifer who in addition to her constant love, support and proof reading has done more to keep me honest about my data and assumptions than anyone else. Thank you all!

Table of Contents

List of Figures

List of Abbreviations

α_w	Absorption coefficient
ω_c	Electron cyclotron angular frequency
ω_p	Plasma frequency
Ω_i	Ion cyclotron angular frequency
τ	Optical depth
κ	Boltzmann's constant
f_c	Electron cyclotron frequency
IREAP	Institute for Research in Electronics and Applied Physics
MCX	Maryland Centrifugal Experiment
UHR	Upper Hybrid Resonance
EBW	Electron Bernstein Wave
DML	Diamagnetic Loop
LGFS	Last Good Flux Surface
GS	Gigasample
eV	Electron Volt
MHD	Magnetohydrodynamic

Chapter 1

Introduction

1.1 Motivation

The Maryland Centrifugal Experiment (MCX) explores the the use of centrifugal confinement toward the goal of controlled nuclear fusion. All fusion experiments seek to confine and heat a plasma to fusion conditions, seeking ion temperatures greater than 100 million degrees Kelvin. Sustaining such high temperatures requires not only efficient heating mechanisms, but also minimizing the rate at which heat is lost to containment vessel. MCX exploits centrifugal force to enhance axial plasma confinement in a magnetic mirror. The basic design of a magnetic mirror is appealing from an engineering and financial standpoint, as the simple coaxial magnet coils are much easier to build and maintain than the more complicated coil arrangements needed for tokamaks, reverse field pinches and stellerators. The cost for this simplification is the open field configuration of magnetic mirrors, meaning that all of the magnetic field lines that pass through the plasma also intersect some part of the containment vessel. In MCX, all field lines corresponding to rotating plasma intersect the ceramic insulators in the mirror throats. Heat loss due to plasma contact with the insulators is a concern both because of the reduced plasma temperature and also because of the potential for large heat fluxes to damage the insulators. Electrons with a given energy move faster, and have a higher collision

rate than the ions so electron heat losses to the insulator will dominate ion losses.

A necessary first step towards measuring the heat loss due to the electrons and evaluating means of limiting this heat loss is measuring the temperature of the electrons. There are several standard methods for measuring the electron temperature in high temperature plasmas, but few of them are suitable for use on MCX. Thompson scattering looks at light scattered by the electrons from a high intensity IR laser and is the most robust method but is prohibitively expensive to set up in an experiment on the scale of MCX. Electron cyclotron emission has become a standard diagnostic for fusion plasmas in tokamaks, where the electron temperature is sufficiently high (1-10 keV) for cyclotron harmonics to be generated, and magnetic field is sufficiently high that the first few cyclotron harmonics may propagate across the plasma to a remote antenna. In MCX the plasma density is high enough that the plasma frequency exceeds the electron cyclotron frequency $\omega_p \gg \omega_c$ in the entire plasma volume so that traditional electron cyclotron measurements are ineffective. The plasma frequency is typically 10 - 100 times greater than the cyclotron frequency so electron cyclotron emission is well below cutoff and will not propagate to an external antenna. Langmuir probes, which consist of a metal wire inserted into the plasma, are another common method and have been attempted, but proved unreliable as a result of significant erosion of the tungsten probe tips by the plasma and a tendency for the alumina jackets to shatter.

Although traditional electron cyclotron measurements are unworkable on MCX, there are two plasma waves which may be thermally excited by the electrons, and which may propagate through an arbitrarily dense magnetized plasma. They are

the right-hand circularly polarized wave, sometimes called the whistler wave, and the electron Bernstein wave. In the MCX plasma both waves are expected to satisfy the blackbody emission condition needed for robust temperature measurements and thus are good candidates for temperature measurements if their emission from the plasma can been seen clearly. In this thesis we will report on experimental investigations on MCX aimed at employing these modes as electron temperature diagnostics. Ultimately, the whistler wave was found to be too difficult to isolate from contaminating emission elsewhere in the plasma and was abandoned as a practical diagnostic. The electron Bernstein wave shows promise as a working diagnostic provided that a robust method of determining the plasma density gradient at the edge of the plasma can be successfully employed.

1.2 Structure of this thesis

Chapter 2 outlines the MCX experimental setup, with a discussion of the primary device, existing diagnostics available and typical operating plasma conditions. Chapter 3 contains a brief treatment of plasma waves using the cold plasma approximation. The dispersion relations for propagation of electromagnetic waves perpendicular and parallel to the magnetic fields are derived and their application to temperature measurements are discussed. Finally, the warm plasma approximation is used to find the dispersion relation for the electron Bernstein wave and the coupling of EBWs to electromagnetic waves will be presented. Chapter 5 describes a series of codes that were developed to compare the observed microwave

emission from MCX to theoretical predictions. Chapter 6 contains the the measured microwave spectra gathered both in the axial (whistler) and radial (EBW) views. The emission in the axial view is shown to be inexplicable from the viewpoint of purely whistler emission, and mode converted EBW emission from the transition region of the plasma is shown to be a likely source of the contaminating emission. Radial EM emission observed at the mid-plane of MCX is shown to be consistent with mode-converted electron Bernstein waves. The detected emission is compared with theoretical predictions for the emitted EBW spectrum and an estimation of the electron temperature is made. Finally the electron heat gain from ion collisions and heat loss at the insulators are estimated and the resulting prediction for the equilibrium electron temperature is found to be in agreement with the estimated electron temperature based on Bernstein emission.

Chapter 2

The Maryland Centrifugal Experiment

2.1 Overview and machine coordinates

In this chapter we will give an overview of the MCX device and the various instruments available to diagnose the plasma. The Maryland Centrifugal Experiment is an innovative confinement experiment that explores the use of centrifugal force and velocity shear to stabilize a magnetic mirror against interchange modes and reduce end-losses. This centrifugal force results from rapid **E x B** rotation driven by a large radial electric field and reduces the end losses which make a standard magnetic mirror unworkable from a fusion standpoint. The sheared flow stabilizes the plasma against interchange modes, resulting in an MHD-stable plasma equilibrium. [1] [2] [3]. A schematic of the MCX experiment is shown in figure 2.1. The radial electric field that initially breaks down the pre-fill gas and drives plasma rotation is provided by the axial high voltage core. Plasma along field lines which terminate on the metallic vacuum vessel is line-tied to the vessel wall and will not rotate, while plasma along field lines which terminate on the insulators is free to rotate at the **E x B** drift speed. The inner and outermost rotating flux surfaces are referred to as the last good flux surfaces (LGFS). The shaped magnetic field, combined with the rapid plasma rotation, produces a centrifugal force which confines the plasma axially to the mid-plane region of the device. Magnetic coils external to

the vacuum vessel may be independently controlled to in order to vary the ratio of the high field at the mirror throat to low the field mid-plane between shots. The ratio of the strongest to weakest on-axis magnetic field defines the mirror ratio, $R_m \equiv B_{max}/B_{min}$.

Locations in the experiment are specified using cylindrical coordinates because of the symmetry of the device. The radius is defined by $r = 0$ at the center of the plasma rotation. The axial location is defined by $z = 0$ at the middle of the machine. The high voltage end refers to the end of the machine where the current is supplied to the center electrode from the capacitor bank. The far end of the machine is referred to as the low voltage end. The magnetic minimum in the center of the device if referred to as the "mid-plane" and contains the hottest and densest plasma. The two magnetic maxima are referred to as the "mirror throats." The transitions between the two are called the "transition regions."

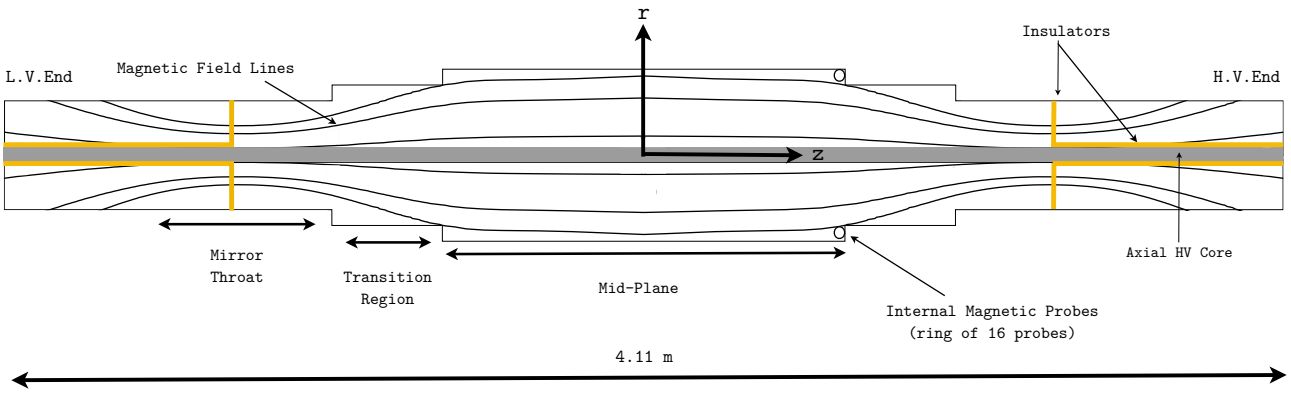

Figure 2.1 – Schematic of MCX illustrating the local coordinate system and commonly referenced locations.

The circuit used to operate MCX is outlined in figure 2.2. For each shot the

capacitor bank is charged to high voltage, typically 10 - 13 kV. The firing ignitron closes the circuit, initiating breakdown of the pre-fill gas and plasma rotation. The plasma rotates, with ionization and plasma temperature maintained by the high electrical current associated with the radial electric field. After a preset time, typically 5 ms ,the plasma discharge is terminated by the crowbar ignitron, which shorts the capacitor bank through the crowbar resistor with a low impedance relative to the plasma. A high power 2 Ω resitor is placed is series with the plasma to provide electrical ballast. Typical operating parameters for MCX are provided in table 2.1

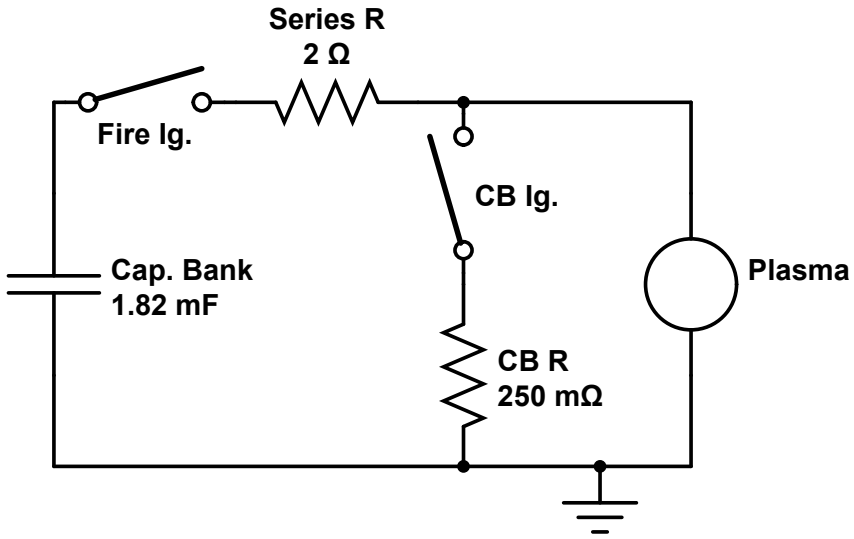

Figure 2.2 – Diagram of the MCX driving circuit.

Based on the measured densities and temperatures in MCX the plasma is essentially fully ionized [4] [5] [6] so the primary means of controlling the plasma density is the pressure of the pre-fill gas, with higher initial pressure leading to higher

plasma densities. The lowest densities that may be reached are on the order of 1 x $10^{19}m^{-3}$; the pre-fill pressures needed for lower densities are too low for avalanche breakdown in the initial electric field. The pre-fill may go as high as 50mTorr before breakdown is no longer possible. However above 7 mTorr the plasma is no longer fully ionized. The highest plasma densities observed around 6 x $10^{20}m^{-3}$.

2.2 Plasma Voltage and Current

The most important diagnostic for MCX is the potential difference measured between the central electrode and the vacuum vessel, referred to as the plasma voltage. Because the stability of the plasma depends critically on the rotation velocity, which is determined by the **E x B** force, the plasma voltage serves as a proxy for the rotation through the relation $v_{plasma} = V/a\mathbf{B}$ where V is the plasma voltage, a is the distance between the innermost and outermost rotating flux surfaces and **B** is the magnetic field. The voltage is measured with a high impedance voltage divider and digitized at 2.5 MHz. Current is measured using a Pearson current transformer. Figure 2.5 shows the plasma voltage and current for a typical discharge. The chamber is pre-filled with 5 mTorr of hydrogen gas. At t = 0.5 ms the firing ignitron switch connects the core to the charged capacitor bank and the electric field breaks down the gas and forms the plasma. The plasma rotates for 5 ms before being terminated by the crowbar ignitron short circuits the core and terminates the discharge. The saw-tooth like oscillation in the plasma voltage is believed to be the result of an m = 2 interchange mode that is only partially stabilized by the sheered

Table 2.1 – MCX dimensions and operational parameters

Mid-plane **B**	0.15 - 0.25T
Mirror Ratio	3 - 10
Mirror to Mirror Length	265 cm
Machine Radius at mid-plane	27 cm
Rotation Velocity	100 - 150 km/s
Mach Number	1 - 4
Pulse Length	5 - 10 ms
Plasma Volume	0.3 m^3
Ion Temperature	100 - 150 eV
Electron Temperature	30 - 100 eV
Plasma Density at $z = 0$	3 - 6 $10^{20}/m^3$
Plasma Voltage	2 - 6 kV
Plasma Current	1 - 3 kA
Capacitor Bank	1.82 mF
Capacitor Voltage	5 - 13 kV
Pre-fill gas	H_2, He, Ag
Pre-fill pressure	0.5 - 50 mT

rotation. [7], [8], [9]

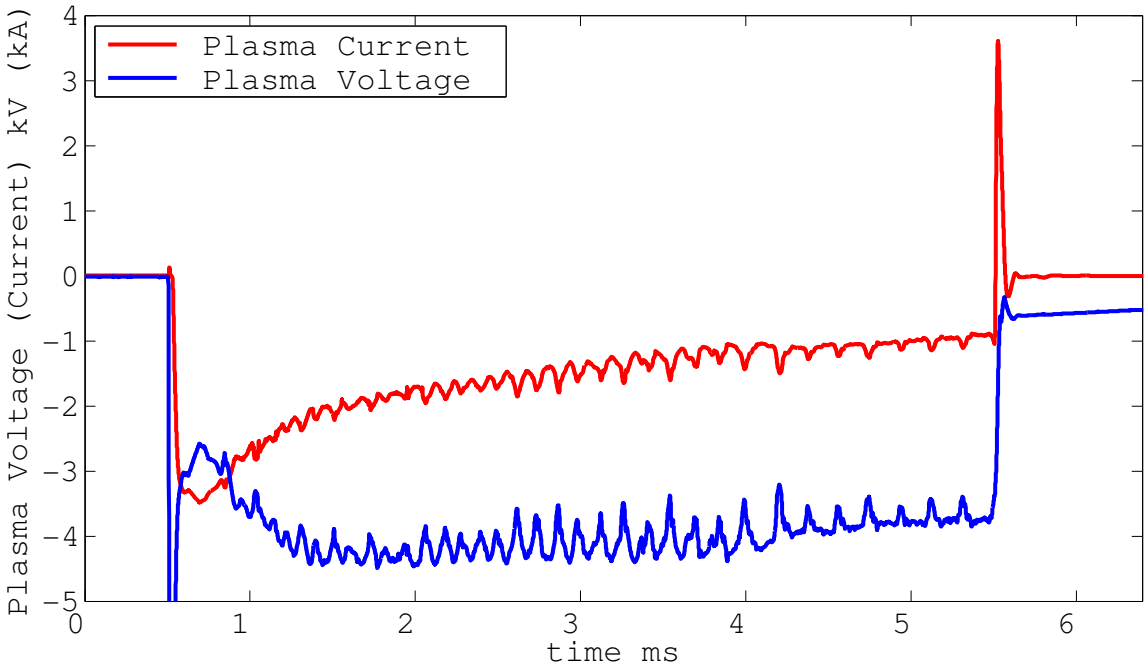

Figure 2.3 – Plasma voltage and current for a typical MCX discharge.

The current shows a saw-tooth pattern associated with the crash in the plasma voltage, with the current increasing as the voltage across the plasma drops. This counterintuitive behavior results from the enhanced cross-field transport of the interchange mode leading to a sudden reduction in the plasma resistivity and resulting in large current across the plasma. The large current reversal at the end of the shot is caused by the rotational kinetic energy of the plasma driving a current through the Pearson transformer into the crowbar resistor. The amplitude and duration of this current reversal provides a diagnostic of the plasma angular momentum at the time of the crowbar. [10] Since the rotational velocity is known from the plasma voltage, the current reversal also measures the total mass of the plasma.

2.3 Magnetic pick-up loops and DMLS

Several magnetic diagnostics are deployed on MCX and measure the bulk plasma pressure and magnetic fluctuations at the edge of the rotating plasma. [11] [8] [9] In this work we will be concerned primarily with an array of 16 magnetic pickup coils that measure rapid fluctuations in the plasma edge. The pickup coils are evenly spaced in a circular array inside the vacuum vessel at z = 66 cm, r = 27 cm (see figure 2.1) and consist of several turns of copper wire, insulated and shielded against electrostatic interference. The probes are oriented to measure changes in the B_z component of the magnetic field. Critically, because the MCX plasma is well magnetized, measuring magnetic fluctuations is equivalent to measuring fluctuations in the edge of the plasma. By correlating the signals from each of the probes in the array the plasma rotation velocity at the edge can be measured as well as the mode structure of the plasma up to m = 7. For the work in this thesis, only half of the coils were used, due to a limited number of digitization channels available for data, limiting the mode resolution to m = 3. Outside of the vacuum vessel an axial array of six diamagnetic loops (DMLs) measure the average change in the axial magnetic field at each of several z locations [11]. The DMLs have limited time response owing to the shielding effects of the steel vacuum vessel. As the plasma forms, the rotating plasma expels magnetic flux, reducing Bz and inducing a voltage in the DMLs. Thus the DMLs give a measure of the kinetic energy of the plasma, and if the rotation speed and temperature are known they also give an estimate of the plasma density. [4]

2.4 Interferometers

Two IR Mach-Zehnder interferometers measure the time resolved, line averaged plasma density at mid-plane and at the transition region. [11] [4] The ratio of the densities measured at these locations gives a direct measurement of centrifugal confinement. The interferometers function well in the higher density conditions when the average plasma density exceeds 1 x $10^{20} m^{-3}$. Below this density the signal to noise ratio approaches unity and the interferometers become susceptible to runaway phase errors that make the interferometers essentially useless for low density measurements.

2.5 Spectrometers

A 10 chord spectrometer measures the emission from the excited states of various impurity ions rotating with the hydrogen plasma. [5] [6] The spectrometer has sufficient spectral resolution to resolve the doppler shift caused by the plasma rotation. By measuring the shift and width of the impurity emission lines the radial velocity profile may be inferred via Abel inversion. [1] Thermal broadening provides a measure of the radial ion temperature profile. The spectrometer can be moved from one series of shots to the other in order to measure the temperature and rotation profiles at mid-plane and also in the transition region.

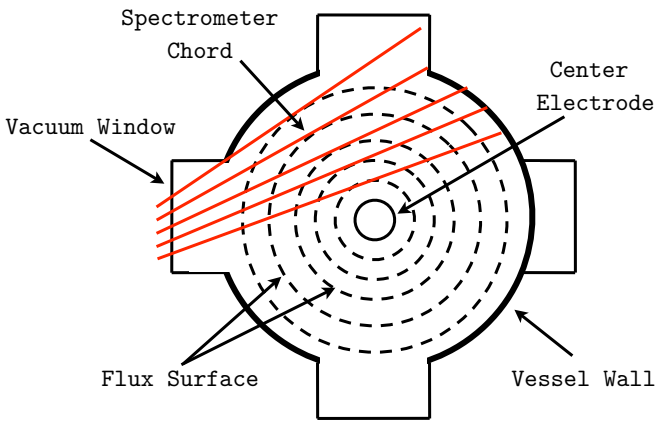

Figure 2.4 – Cutaway of the MCX mid-plane showing the spectrometer chords used to measure the plasma rotation and ion temperature profiles. Only 5 chords out of the full 10 are shown for clarity.

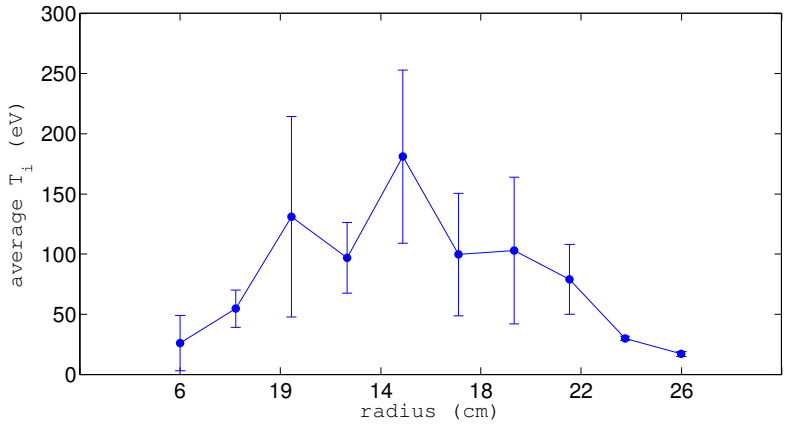

Figure 2.5 – Ion temperature as a function of radius measured using thermal doppler broadening spectroscopy. [6]

Chapter 3

Plasma Waves and Radiation Transport

3.1 Overview

Observation of electron cyclotron emission (ECE) has become a standard and reliable means of measuring the electron temperature in fusion plasmas. [12] [13] [14] The electrons orbiting their gyrocenters emit and absorb radiation at the cyclotron frequency and its harmonics. If the optical depth of the plasma at these frequencies sufficiently high ($\tau > 2$), the emission intensity is a function only of the electron temperature and the plasma is said to emit as a blackbody. For a plasma in a spatially inhomogeneous magnetic field this technique provides a non-perturbative means to measure the localized electron temperature. The situation is complicated when some or all of the plasma is overdense ($\omega_p \gg \omega_c$). Then all but the high harmonics of the cyclotron frequency are cutoff and do not propagate through the plasma. In a typical MCX discharge $\omega_p/\omega_c \sim 20$ and practically the entire plasma volume is overdense. There are two modes which may still propagate through an overdense plasma, the right-hand circularly polarized (RCP) wave and the Electron Bernstein Wave (EBW). [13]

The RCP wave, sometimes referred to as the whistler wave, is an electromagnetic mode which propagates parallel to the magnetic field in an overdense plasma at frequencies below ω_c. In a magnetic mirror such as MCX these waves originate in

the interior of the plasma and propagate axially along the magnetic field mode converting to pure electromagnetic waves as they exit the plasma and may then be detected by an antenna. The whistler mode has been used successfully in non-rotating magnetic mirror experiments to measure electron temperatures. [15] [16] [17] [18]

The electron Bernstein wave is an electrostatic mode which may mode convert to an electromagnetic wave if it encounters an upper hybrid resonance (UHR) near the edge of the plasma. The optical depth for the EBW is expected to be quite large and the wave easily achieves blackbody emission, making it an attractive candidate for temperature measurements provided the details of this mode conversion process are known.

In this chapter we outline the physics behind temperature measurements using ECE. First we discuss the absorption, emission and transport of radiation through a plasma and discuss the concepts of optical depth and blackbody emission. Then we examine the dispersion relation for waves in the cold plasma approximation and discuss the utility of these waves as temperature diagnostics. Finally warm plasma theory is used to find the dispersion relation and absorption coefficient for the EBW and the details of mode conversion to electromagnetic modes are considered.

3.2 Radiation transport, optical depth and measurement

Consider an antenna viewing a large slab of plasma of width L and temperature T. The plasma within the slab is both emitting and absorbing radiation. The specific intensity $I(\omega)$ emerging from the plasma is given by [13]

$$I_\omega = I_{\omega 0} e^{-\tau} + \int_0^\tau S_\omega(\tau)\, e^{-\tau} dx \tag{3.1}$$

where τ is the optical depth defined by,

$$\tau = -\int_0^L \alpha_\omega \, dx \tag{3.2}$$

$S_\omega(\tau)$ is the source function and α_ω is the absorption coefficient defined as $\alpha_\omega = -2\,\mathrm{Im}(k)$. The $I_{\omega 0}$ term describes radiation from a source behind the plasma being partially absorbed as it traverses the plasma. In general, $S(\omega, \tau)$ may be a complicated function of the plasma parameters. However, if the plasma is in local thermodynamic equilibrium at temperature T and has a distribution function that can be approximated by a Maxwellian then the source function can be written as, [13]

$$S(\omega, \tau) = \frac{\omega^2}{8\pi^3 c^2} \kappa T \tag{3.3}$$

where k_B is Boltzmann's constant. With the source function known the intensity from the slab as a function of temperature and absorptivity becomes,

$$I(\omega) = (\frac{\omega^2}{8\pi^3 c^2}) \kappa T (1 - e^{-\tau}) \tag{3.4}$$

If the optical depth is high, ($\tau \gg 1$) then the plasma is said to be optically thick and emits like a blackbody. If the the optical depth is low ($\tau \ll 1$) then the plasma is optically thin and details such as the finite extent of the plasma, background sources of emission and reflecting walls must be taken into account.

In either case (3.4) predicts the emitted intensity provided that the absorption coefficient, and thus the optical depth, is known. The absorption coefficient may be calculated either from knowledge of the Einstein Coefficients for the medium, or through the dispersion relation for the wave. In this work, the dispersion relation is used exclusively.

3.3 Waves in a cold plasma

The cold plasma approximation is used to find the dispersion relations for waves in plasmas where the thermal motion of the particles does not contribute significantly to the physics. In this approximation the particles are assumed to have no thermal motion, only the motion corresponding to the waves is considered. As such, the cold plasma approximation does not contain collisions, relativistic effects, Landau damping or finite Larmour radii. While this clearly leaves out a great deal of physics, the model has had great success in explaining solar and ionospheric waves and is of great utility for predicting the overall behavior of electromagnetic waves even in fusion plasmas. [19] As a further simplification, because only waves where $\omega \gg \Omega_i$ are considered, the ions are assumed to be motionless from the beginning. We begin by solving Maxwell's equations for the electron dispersion relation.

$$\nabla \times \mathbf{B} = \mu_0 \mathbf{J} + \mu_0 \epsilon_0 \mathbf{E} \tag{3.5}$$

$$\nabla \times \mathbf{E} = -\frac{\partial \mathbf{B}}{\partial t} \tag{3.6}$$

After Fourier transforms in time and space, these equations can be combined and rearranged to yield,

$$(\mathbf{kk} - k^2\mathbf{I} + \frac{\omega^2}{c^2}\mathbf{K}) \cdot \mathbf{E} = 0 \tag{3.7}$$

with $\mathbf{K} = \mathbf{I} + i\boldsymbol{\sigma}/\epsilon_0\omega$ the dielectric permittivity and $\mathbf{I}, \boldsymbol{\sigma}$ the identity and conductivity tensors. The fluid equation for the plasma, neglecting collisions and ions is,

$$nm\frac{d\mathbf{v}}{dt} = nm\left(\frac{\partial \mathbf{v}}{\partial t} + \mathbf{v} \cdot \nabla \mathbf{v}\right) = nq\left(\mathbf{E} + \mathbf{v} \times \mathbf{B}\right) - \nabla\Phi \tag{3.8}$$

where Φ is the fluid stress tensor. Since thermal effects can be ignored, the components of the stress tensor will be small compared to the other terms in (3.8) and can be dropped.

Defining a coordinate system with z parallel to the magnetic field, the cold plasma fluid equations may be used to obtain an expression for the dielectric tensor, [19]

$$\boldsymbol{\epsilon} \cdot \mathbf{E} = \begin{pmatrix} S & -iD & 0 \\ iD & S & 0 \\ 0 & 0 & P \end{pmatrix} \begin{pmatrix} E_x \\ E_y \\ E_z \end{pmatrix} \tag{3.9}$$

$$S = \frac{1}{2}(R + L), \qquad D = \frac{1}{2}(R - L) \tag{3.10}$$

$$R \equiv 1 - \frac{\omega_p^2}{\omega(\omega + \omega_c)} \tag{3.11}$$

$$L \equiv 1 - \frac{\omega_p^2}{\omega(\omega - \omega_c)} \tag{3.12}$$

$$P \equiv 1 - \frac{\omega_p^2}{\omega^2} \tag{3.13}$$

For simplicity, we restrict our attention to waves propagating either parallel or perpendicular to the magnetic field. Casting the wave equation as

$$\mathbf{n} \times (\mathbf{n} \times \mathbf{E}) + \boldsymbol{\epsilon} \cdot \mathbf{E} = 0 \tag{3.14}$$

and defining θ as the angle between the magnetic field and the direction of propagation for the wave we find that the general dispersion relation can be written as,

$$\tan^2(\theta) = \frac{-P(n^2 - R)(n^2 - L)}{(Sn^2 - RL)(n^2 - P)} \tag{3.15}$$

This allows easy specilization to the case of waves moving either parallel to ($\theta = 0$) or perpendicular ($\theta = \pi/2$) to the magnetic field.

3.4 Propagation parallel to the magnetic field

Substituting $\theta = 0$ into (3.15) then we find that there are two possible branches corresponding to the right hand circularly polarized (RCP) and left hand circularly polarized (LCP) mode. Their dispersion relations are given by,

$$k_{RCP}^2 = \left(\frac{\omega^2}{c^2}\right)\left(1 - \frac{\omega_p^2}{\omega^2 - \omega_p\omega}\right) \tag{3.16}$$

$$k_{LCP}^2 = \left(\frac{\omega^2}{c^2}\right)\left(1 - \frac{\omega_p^2}{\omega^2 + \omega\omega_p}\right) \tag{3.17}$$

The RCP mode has a resonance at $\omega = \omega_c$ and a cutoff at right hand cutoff, $\omega_R = \frac{1}{2}[\omega_c + \left(\omega_c^2 + 4\omega_p^2\right)^{\frac{1}{2}}]$. The LCP mode has a cutoff at the the left hand cutoff, $\omega_L = \frac{1}{2}[-\omega_c + \left(\omega_c^2 + 4\omega_p^2\right)^{\frac{1}{2}}]$. These dispersion relations are shown graphically in Figure 3.1 If the plasma is overdense then the LCP mode is beyond cutoff and cannot propagate through the plasma. However, the RCP mode may propagate at frequencies below ω_p so long as the frequency is also below ω_c.

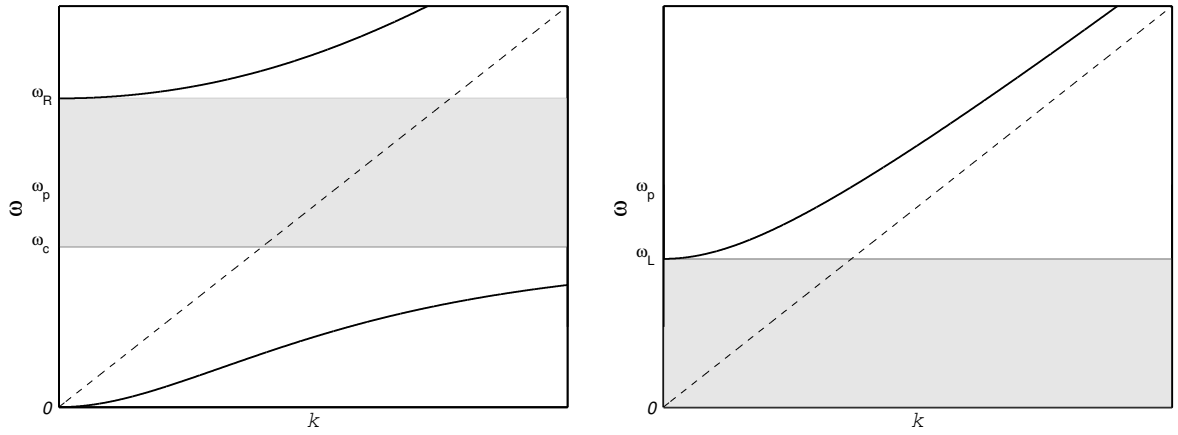

(a) RCP wave **(b)** LCP wave

Figure 3.1 – The dispersion behavior for waves in a cold plasma propagating parallel to the magnetic field, with ion motions ignored. The shaded areas indicate regions where there is no propagation. The dashed line corresponds to vacuum propagation. Note that the RCP wave may propagate at frequencies below ω_p.

The ability of the RCP wave to propagate even at very high densities makes it

an attractive candidate for temperature diagnostics on a device like MCX. Because MCX has an axially inhomogeneous magnetic field, the electrons at different axial locations are resonant over a large range of frequencies. Radiation emitted from these resonant zones is free to propagate along the magnetic field line toward the mirror throat since $\omega < \omega_c$ is satisfied at all points along this path. Reabsorption after the magnetic maximum is not a concern because the plasma is terminated at the magnetic maximum by the ceramic insulator. Once the wave reaches the ceramic insulator it will mode convert to ordinary microwave radiation and propagate to a receiving horn on the other side of the insulator. Radiation detected behind the insulator at a frequency f corresponds to emission from an axial location in the magnetic mirror where $f = f_c$. Scanning the received frequency is then equivalent to scanning different axial locations. This simple picture is complicated by the wave transmission through the ceramic insulator which consists of several concentric ceramic tubes with a radial spacing which is on the same order as the wavelength of the cyclotron emission and has been partially metallized by vapor produced by the plasma discharge. These complications will be considered in more detail in Chapter 6.

3.5 Propagation perpendicular to the magnetic field

Looking at (3.15) and setting $\theta = \pi/2$ there are again two branches for the dispersion relation, corresponding to polarization parallel or perpendicular to the magnetic field. The two modes are usually referred to as the extraordinary (X)

mode and the ordinary (O) mode. The X-mode wave is polarized with the **E**-field perpendicular to the magnetic field, while the O-mode has **E** parallel to the magnetic field. The dispersion relations are given by, [13]

$$k_o^2 = \left(\frac{\omega^2}{c^2}\right)\left(1 - \frac{\omega_p^2}{\omega^2}\right) \tag{3.18}$$

$$k_x^2 = \left(\frac{\omega^2}{c^2}\right)\left(1 - \frac{\omega_p^2}{\omega^2}\frac{\omega^2 - \omega_p^2}{\omega^2 - \omega_h^2}\right) \tag{3.19}$$

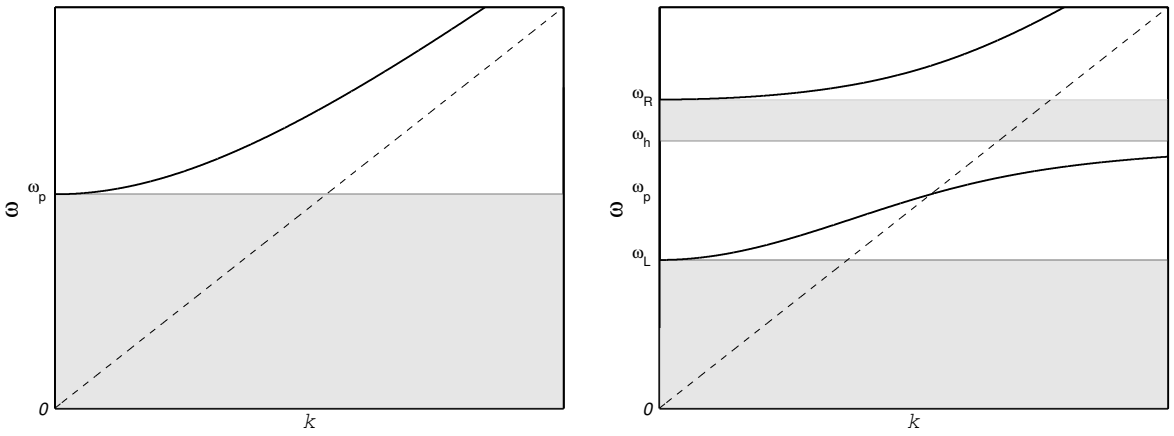

(a) O-mode wave **(b)** X-mode wave

Figure 3.2 – The dispersion behavior for waves in a cold plasma propagating perpendicular to the magnetic field, with ion motions ignored. The shaded areas indicate regions where there is no propagation. The dashed line corresponds to vacuum propagation.

where $\omega_h = \sqrt{\omega_p^2 + \omega_c^2}$ is the upper-hybrid frequency. The behavior of the O-mode is straight forward; if $\omega_p \gg \omega$ the the radiation is beyond cutoff and does not propagate. The X-mode is more complex, containing two cutoffs and a resonance.

The plasma in MCX is sufficiently overdense that the X-mode is cutoff in practically the entire plasma volume so this mode does not offer any direct means of making temperature measurements. However, there is the possibility for the X-mode to couple to the electron Bernstein mode at the upper hybrid resonance. The Bernstein wave does not appear in the cold plasma model, because it involves the gryo-motion of the electrons, which is neglected in the cold plasma treatment. In order to see the physics of the Bernstein wave, the warm plasma dielectric tensor must be employed.

3.6 Electron Bernstein Waves

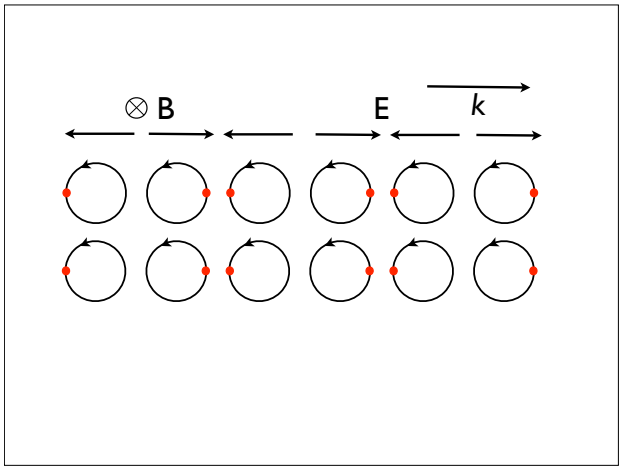

Figure 3.3 – The electron Bernstein mode. The wave motion is perpendicular to the external magnetic field with a wavelength close to four times the gyroradius.

The electron Bernstein wave is an electrostatic mode that consists of coherent motion of the electrons about their guiding centers. The key features of this mode that make it an attractive candidate for temperature diagnostics are that it may

propagate in an over-dense plasma and that it is strongly absorbed at harmonics of the cyclotron frequency. The EBW has extremely short wavelengths compared to many other plasma waves, with $\lambda \sim 4r_c$ so that EBWs easily achieve high optical depths in even modest laboratory plasmas. Because Bernstein waves are electrostatic ($\mathbf{k} \times \mathbf{E} = 0$) they cannot directly couple to a vacuum mode and travel from the plasma to a receiving antenna. Fortunately, it is possible for Bernstein waves to couple to the X-mode at the upper hybrid resonance, where the X-mode wavelength approaches the scale of the electron gyroradius. To find the dispersion relation for the EBW the electrostatic nature of the wave can be exploited to simplify the analysis by equating the electric field E with the gradient of a scalar $\phi(\mathbf{r}, \mathbf{t})$. First, from Maxwell's equations we have,

$$\nabla \cdot (\nabla \times \mathbf{B}) = 0 \tag{3.20}$$

$$\nabla \cdot \left(\mu_0 \mathbf{J} + \mu_0 \epsilon_0 \frac{\partial \mathbf{E}}{\partial t} \right) = 0 \tag{3.21}$$

then making use of $\mathbf{E} = -i\mathbf{k}\phi$,

$$i\mathbf{k} \cdot (-i\omega \boldsymbol{\chi} \cdot \mathbf{E} - i\omega\epsilon_0 \mathbf{E}) = 0 \tag{3.22}$$

$$i\mathbf{k} \cdot (\omega \boldsymbol{\chi} \cdot \mathbf{k}\phi + \omega\epsilon_0 \mathbf{k}\phi) = 0 \tag{3.23}$$

$$\mathbf{k} \cdot \boldsymbol{\chi} \cdot \mathbf{k} + \epsilon_0 k^2 = 0 \tag{3.24}$$

$$\mathbf{k} \cdot \boldsymbol{\epsilon}(\omega, \mathbf{k}) \cdot \mathbf{k} = 0 \tag{3.25}$$

For a coordinate system with the magnetic field in the z-direction, and a plasma with a Maxwellian velocity distribution then the hot plasma dielectric tensor is given by, [19] [20]

$$\boldsymbol{\epsilon} = \mathbf{1} + \frac{\omega_p^2}{\omega^2}\zeta_0 \sum_{n=-\infty}^{\infty} \begin{pmatrix} \frac{n^2}{\mu}\tilde{I}_n Z_n & in\tilde{I}'_n Z_n & -n\sqrt{\frac{2}{\mu}}\tilde{I}_n\left(1+\zeta_n Z_n\right) \\ -in\tilde{I}'_n Z_n & \left(\frac{n^2}{\mu}\tilde{I}_n - 2\mu\tilde{I}'_n\right) Z_n & i\sqrt{2\mu}\tilde{I}'_n\left(1+\zeta_n Z_n\right) \\ -n\sqrt{\frac{2}{mu}}\tilde{I}'_n\left(1+\zeta_n Z_n\right) & -i\sqrt{2\mu}\tilde{I}'_n\left(1+\zeta_n Z_n\right) & 2\zeta_n\tilde{I}_n\left(1+\zeta_n Z_n\right) \end{pmatrix} \tag{3.26}$$

where $\zeta_n = (\omega + n\omega_c)/(|k_z^2|v_{th}^2)$, $\tilde{I}_n = e^{-\mu} I_n(\mu)$, $\mu = k_\perp^2 v_{th}^2/(2\omega_c^2)$, I_n is the n^{th} order modified Bessel function and Z is the plasma dispersion function

$$Z(\zeta_j) = \frac{1}{\sqrt{\pi}} \int_{-\infty}^{\infty} \frac{e^{-s^2}}{s - \zeta_j} ds \tag{3.27}$$

With this dielectric tensor, (3.25) can be solved for the EBW dispersion relation. The condition for nontrivial solutions to (3.25) is that the determinate of the dielectric tensor vanish. For the case of a wave traveling perpendicular to the magnetic field this can be shown to reduce to [13]

$$0 = 1 - 2\left(\frac{\omega_p}{\omega_c}\right)^2 \sum_{n=1}^{\infty} I_n(\lambda) \frac{e^{-\lambda}}{\lambda} \frac{n^2}{(\omega/\omega_c)^2 - n^2} \tag{3.28}$$

Here, $\lambda = (k_\perp v_0/\omega_c)^2$. Figure 3.4 shows the solutions to (3.28) for several plasma densities and shows vividly that the wave is absorbed at harmonics of the

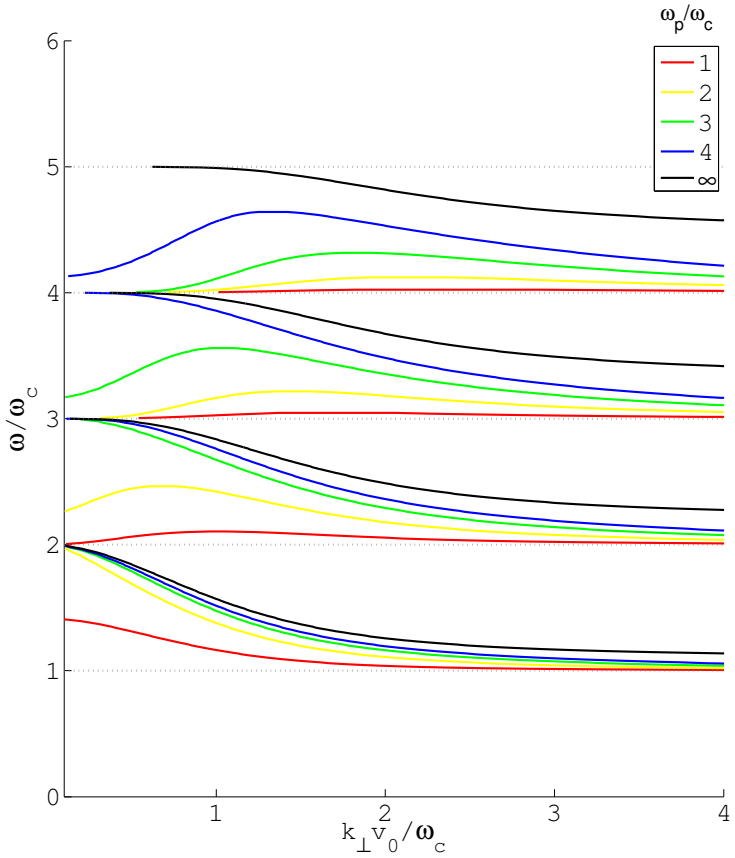

Figure 3.4 – Dispersion Relation for the electron Bernstein wave moving perpendicular to the magnetic field in a thermal plasma.

cyclotron frequency. While (3.28) is useful in illustrating the cutoff and resonance behavior of the EBW, it does not allow for solutions with with k_r and k_i simultaneously larger than zero, a condition needed for absorption, so it is not useful in calculating the optical depth for an EBW. To enable calculation of the optical depth, Bornatici *et al* [21] derived a dispersion relation that includes weak relativistic effects and is valid in the vicinity of a resonance. The dispersion relation is,

$$k = \frac{\omega_c}{v_{th}} \left(\frac{1}{\sqrt{2\pi}} \frac{\omega_p}{\omega_c}^{1/3} \mu \right)^{1/3} \left[F_1 \left(z_n - \frac{\mu n_\parallel^2}{2} \right) \right]^{1/3} \tag{3.29}$$

$$F_1 = \begin{cases} e^x E_1(x) & : x > 0 \\ -e^x [E_1(-x) + i\pi] & : x > 0 \end{cases} \tag{3.30}$$

Here $E_1(x)$ is the exponential integral function, $z_n = \mu(1 - n\omega_c/\omega)$ and $\mu = (c/v_{th})^2$. This relation is valid for propagation that is nearly perpendicular to the magnetic field ($n_\parallel < v_{th}/c$) and allows a calculation of the absorption coefficient for the EBW. Figure 3.5 shows the solution to (3.29) across the second harmonic resonance for plasma conditions similar to those expected in the MCX plasma. Integration of -2Im(k) across the resonance yields the optical depth τ. For densities on the order of a few $10^{20} m^{-3}$ and temperatures between 30 - 100 eV the optical depth for the 2nd cyclotron harmonic at the MCX in the hundreds, easily reaching blackbody emission.

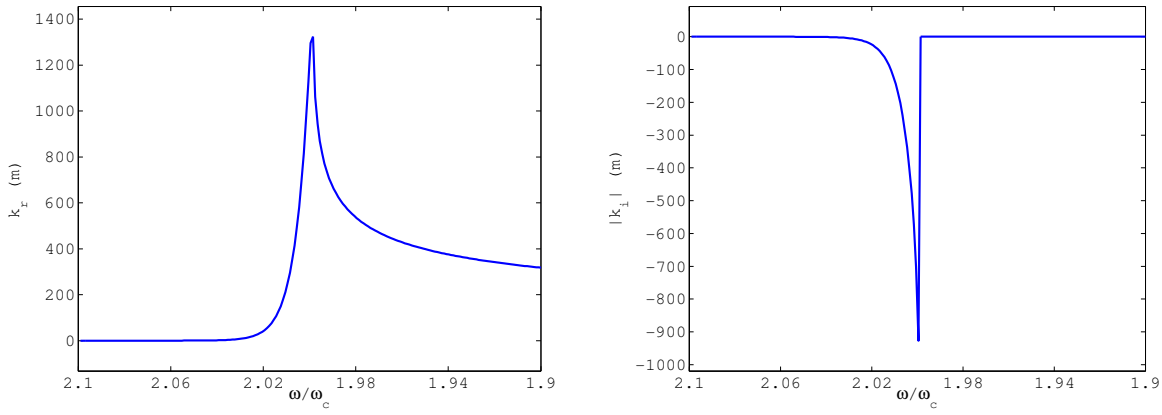

Figure 3.5 – Real and imaginary wave numbers of an EBW calculated near the second harmonic of the cyclotron frequency for realistic conditions similar to those expected in the interior of the MCX plasma: $n = 1 * 10^{20}/m^3$, Te = 90 eV, B = 0.2T.

3.7 Coupling of the Bernstein Mode to the X-mode

The EBW is an attractive candidate for electron temperature measurements on MCX because the optical depth is large, ensuring blackbody emission, and because there is no limit to propagation from the high density. The complicating factor in the use of EBWs for temperature measurements is that the EBW mode is electrostatic and cannot propagate outside of the plasma, making direct detection impossible. All detection schemes for EBWs revolve around the EBW mode converting to an electromagnetic wave which may then exit the plasma and be detected. When an EBW propagates toward the plasma boundary it may encounter a UHR layer, which is also a resonance of the cold plasma X-mode, where the X-mode's wavelength is approaching zero and is on the order of the electron gryoradius. At the UHR the two waves are indistinguishable and one may mode convert to the other. The details

of this coupling have been studied in some detail, [22], [23], [24] and experimental detection of this emission has been used successfully as a temperature diagnostic on totamaks, spherical tokamaks and stellerators [25], [26] and the reverse process has been employed for RF heating of over-dense plasmas and RF current drive. For a review of the subject as it applies to fusion experiments see [20].

There are two possible schemes for coupling an RF wave from the outer, (underdense) plasma to the EBW in the inner (overdense) plasma. In the first scenario an O-mode is launched toward the plasma at an angle to the magnetic field such that the O-mode cutoff occurs at the same position as the slow X-mode cutoff which allows the O-mode to convert into a slow X-mode wave which then converts to an EBW at the upper-hybrid resonance. This process is usually referred to as the O-X-B mode conversion process and has been used for both temperature diagnostics and electron heating on the W7-AS stellerator. [20] The O-X-B mode conversion scheme is quite sensitive to the angle between the incoming O-mode and the magnetic field. No investigation of this process has been done on MCX, it here for completeness.

The second method involves launching a fast X-mode wave perpendicular to the magnetic field. The fast X-mode tunnels past the right hand cutoff and couples to the slow X-mode which then mode converts to an EBW at the UHR. This coupling process is referred to as direct, or X-B coupling, and is highly dependent on the density gradient at the UHR. The process is illustrated in figure 3.6.

The process begins with a fast X-mode propagating from vacuum into an overdense plasma. If the density gradient is sufficiently steep then the wave tunnels past the right hand cut-off and couples to the slow X-mode. The slow wave con-

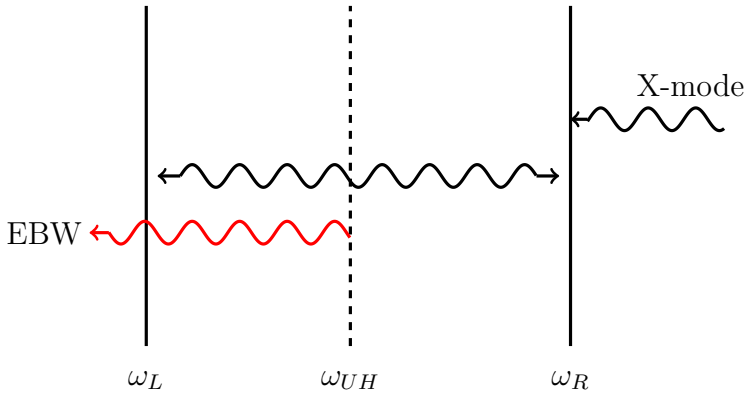

Figure 3.6 – The X-B mode conversion process. An X-mode approaches from the right and tunnels past the righthand cutoff to the UHR where it partially converts to an EBW. The remaining X-mode reflects from the lefthand cutoff. The combination of two cutoffs enclosing a resonance acts as a lossy resonant cavity.

tinues until it reflects off of the lefthand cutoff and propagates to the UHR where it partially mode-converts to the EBW. The remaining slow wave reflects back off of the righthand cut-off. In the proximity of the cutoffs and resonance, wavelength is poorly defined and the WKB solutions of the wave equation are not applicable. This configuration of a resonance contained between two cutoffs has been shown to behave as a lossy resonance cavity, with mode conversion to EBWs providing the loss mechanism [22], where it was also shown that for certain frequencies and density gradients the mode conversion efficiency can be as high as 100%. The mode conversion efficiency C is given by [22]

$$C = 4e^{-\pi\eta}\left(1 - e^{-\pi\eta}\right)\cos^2\left(\frac{\phi}{2} + \theta\right) \tag{3.31}$$

$$\eta = \frac{\omega_c L_n}{c} \frac{\alpha}{\sqrt{\alpha^2 + 2\left(L_n/L_B\right)}} \left(\frac{\sqrt{1+\alpha^2} - 1}{\alpha^2 + \left(L_n/L_B\right)\sqrt{1+\alpha^2}} \right)^{1/2} \tag{3.32}$$

$$\alpha = \frac{\omega_p}{\omega_c} \tag{3.33}$$

$$L_n = \frac{n_e}{\partial n_e / \partial x} \tag{3.34}$$

$$L_B = \frac{B}{\partial B / \partial x} \tag{3.35}$$

$$\theta = \text{phase}\left(\Gamma\left(-i\pi\eta\right)\right) \tag{3.36}$$

with ϕ being the phase difference between the slow X-mode propagating toward the L-cutoff and the reflected wave propagating back towards the UHR. Note that in (3.31) - (3.35), all quantities are evaluated at the UHR. Near the UHR in MCX we expect that $L_n << L_B$ and $\omega_p \sim \omega_c$. Applying these limits to (3.32) we find that the parameter η is approximately given by,

$$\eta \simeq \frac{1}{2}\left(\frac{\omega_c L_n}{c}\right) \tag{3.37}$$

which highlights the strong dependance of the coupling efficiency on the density scale length. While (3.37) gives a good qualitative description for the mode conversion efficiency, in all numerical calculations done in this work the full expression for L_n is used. Figure 3.7 shows the maximum efficiency as a function of

the density scale length for conditions expected near the UHR in MCX. As can be clearly seen, efficient mode conversion requires a very steep density gradient.

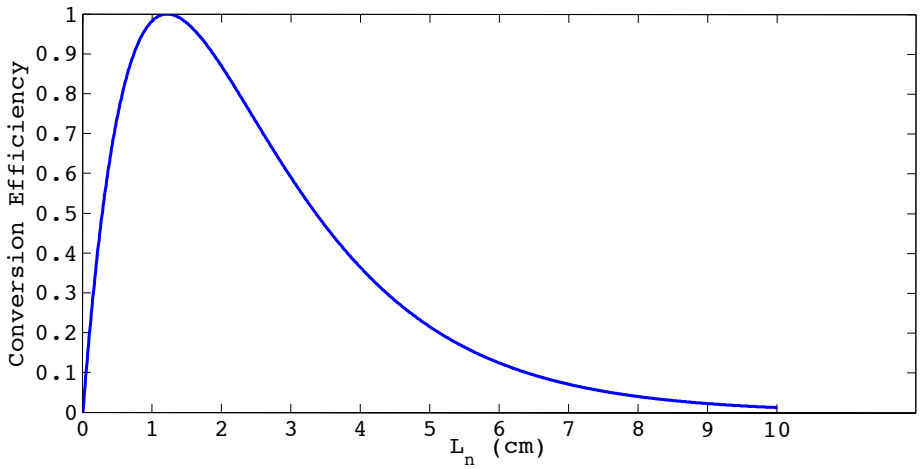

Figure 3.7 – Maximum efficiency of the mode conversion between the electron Bernstein wave and the X-mode as a function of the density scale L_n. The upper hybrid frequency for this calculation is 11.3 GHz.

Chapter 4

Diagnostic Set Up

4.1 Overview

The bulk of the plasma in MCX is known to be overdense in the full range of cyclotron frequencies, and therefore most of the cyclotron radiation generated by the electrons is trapped within the plasma and cannot escape to reach an observing antenna. As outlined in chapter 3, however, there are two modes that may propagate through an over-dense plasma and offer some hope of giving meaningful information about the electron temperature. The whistler mode, which propagates parallel to the magnetic field, and the Bernstein mode which may couple to the fast X-mode and escape the plasma. Both of these modes are expected to reach black body emission in the MCX plasma and may be useful diagnostics if their emission can be observed cleanly. In this chapter we will describe the experimental apparatus that were used in MCX to measure the axial and radial microwave emissions as well as a array of electrostatic probes employed to measure fluctuations in the plasma density in the edge of the mid-plane plasma.

4.2 Radiometers

Two radiometers were constructed, operating in the Ka-band (26.5-40.0 GHz) and the X-band(8.2-12.4 GHz). These frequency bands correspond to the fundamen-

tal cyclotron resonances in the mirror throat and transition regions of the plasma. The X-band radiometer may also be used to observe frequencies around the 2nd cyclotron harmonic at mid-palne. The microwave signals are received by rectangular pyramidal horns that are sensitive to polarization. The received wave is passed to the radiometer using standard WR - 90 (X - band) and WR - 28 (Ka - band) metallic wave guides, passing through the vacuum vessel via commercial mica pressure windows. To isolate the radiometers from electrostatic interference the waveguides are brazed to vacuum vessel wall at the feedthrough, ensuring that the waveguide stays at the same potential as the vessel. Ground loops are prevented by placing a sheet of Kapton, .002" thick between two adjacent waveguide segments, secured with nylon screws, to avoid forming a conducting path from the vessel to the radiometer ground.

The received signals are amplified and mixed with a local oscillator signal using double-balanced mixers and filtered to produce the 60 MHz intermediate frequency (IF) signals that can then either be digitized directly using a 2 GS/s oscilloscope or passed to an IF detector that produces a voltage proportional to the amplitude of the IF signal. The fast scope provides the best resolution of the signal, but produces large data files (2 GByte/shot). The IF detector is limited by the resolution of the MCX digitizers to 2.5 MHz, but produces smaller data files and is automatically synchronized with most of the other diagnostics. In particular, the voltage, current and magnetic probes use the same digitizer. The initial amplifier for the Ka-band radiometer limits its use to 30.0 - 40.0 GHz.

The radiometers are constructed entirely of legacy equipment, and instrument

specifications are unfortunately no longer available for virtually all of the components. To produce usable data the radiometers are calibrated using commercial solid state, standard noise sources, which produce microwave noise with a known intensity across a broad frequency range. The noise sources were produced by Advanced Technical Materials (ATM), and are described in table 4.1

Table 4.1 – Calibrated noise source characteristics

X-band			Ka-band		
Freq. (GHz)	ENR	Eff. Temp. (eV)	Freq. (GHz)	ENR	Eff Temp. (eV)
8.00	28.00	15.75	33.5	8.00	0.13
9.00	28.45	17.47	34.5	8.00	0.13
10.00	28.86	19.23	35.5	7.90	0.13
11.00	28.87	19.24	36.5	8.00	0.13
12.0	28.86	19.23	37.5	8.00	0.13
			38.5	8.00	0.13
			39.5	8.10	0.14

The calibration noise from these sources is passed to the radiometers via SMA to waveguide adapters, allowing calibration of the entire detector system, including pressure windows and waveguide runs for every configuration. The X-band noise source does not output uniform power across the entire band of interest but instead falls off at low frequencies. Because only a limited number of calibration points are

provided by ATM an empirical formula is used to interpolate between these points. The formula, $19.23 \tanh(0.6f - 3.7)$ is found to reproduce the given calibration points to within 3 percent and is used in calibrating the X-band receiver. The calibration was done after allowing time for the noise source and radiometer to warm up to a stable temperature and repeated on two different days to ensure the stability of the measurements. The sensitivity is not entirely flat, showing greatly reduced sensitivity between 10.7 - 11.8 GHz. The reason for this nonuniformity is unknown, however, it is consistent across all calibration measurements and is straight-forward to compensate for when analyzing the X-band data. The calibration for the X-band receiver connected to the radial waveguide run is shown in figure 4.1

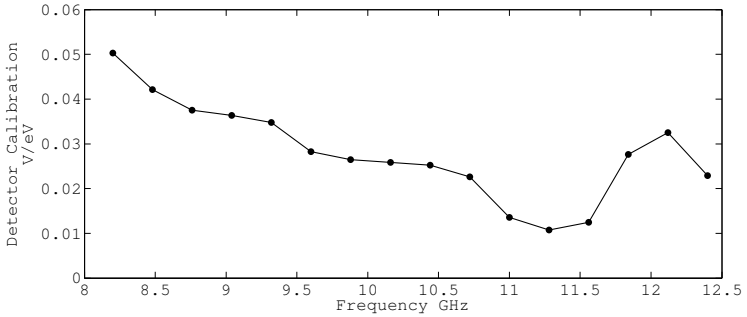

Figure 4.1 – The X-band detector response measured using the solid state noise source. Error bars are within the point markers.

4.3 Axial View

The axial view configuration is used to measure emission emerging parallel to the magnetic field in the whistler mode. In this configuration the Ka- and X-band horns are mounted behind the main insulator, as close to the alumina as possible

so as to minimize the distance between the horns and the plasma on the other side of the insulators. The vacuum feed-thoughs are mounted on rotatable flanges so that the horns can be rotated in order to check the polarization of the microwaves. In this configuration the viewing pattern of the horns is a significant concern; the radiation is viewed through the alumina insulator which is made of nested coaxial alumina cylinders. The spacing between these cylinders is comparable to the vacuum wavelengths of the Ka-band, and the plasma facing edges of the alumina have been partially metallized by repeated exposure to the plasma. These features give the insulator the potential to scatter the microwaves, making it harder to isolate the source of the signal. Reflections from the wall and the core also pose serious concerns as signals from unexpected regions of the plasma may arrive at the horn after a series of reflections from the vessel walls and the overdense plasma.

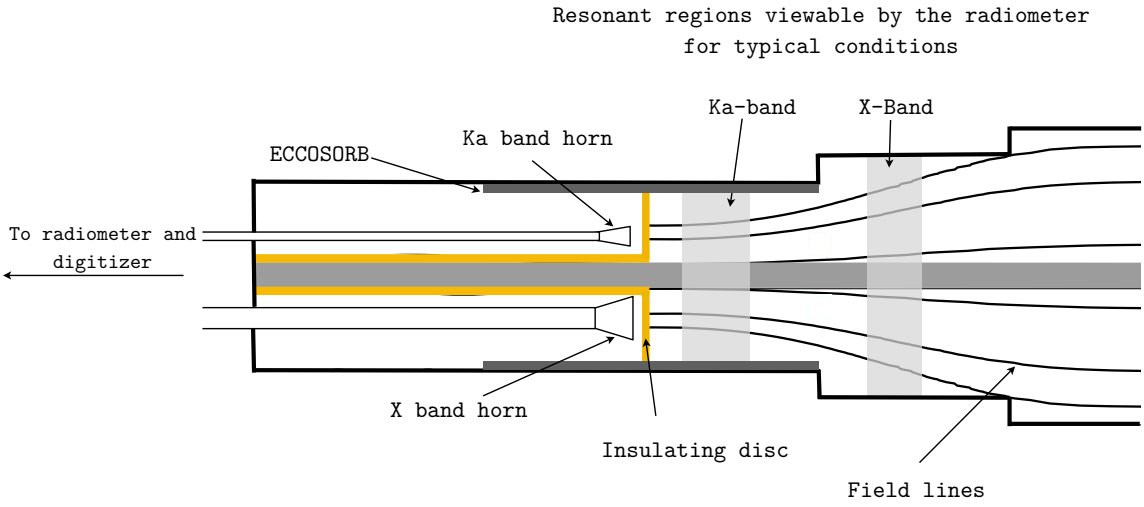

Figure 4.2 – The horns mounted axially to view radiation in the whistler mode.

Reflections from the wall can be reduced by lining some of the walls with

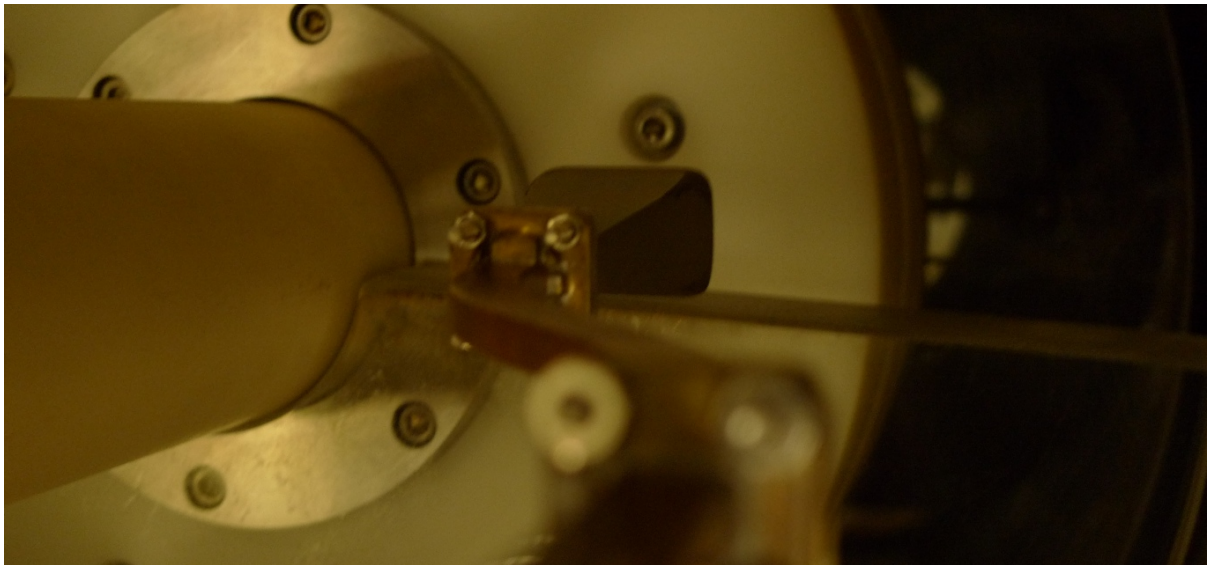

Figure 4.3 – The Ka-band horn mounted behind the main insulator, the X - band horn is mounted with a parallel view on the other side of the core.

ECCOSORB®, which is a commercial product used to absorb stray microwaves in order to mitigate reflections. This technique is only of limited use because ECCOSORB® is made from a carbon loaded polymer and will not tolerate contact with even the relatively mild plasma near the rotating edge. For this reason only the walls well removed from the plasma can be covered. ECCOSORB® also has a porous structure, and therefore a large surface to mass ratio which increases outgassing, lengthening the pump down time and increasing the concentration of impurity ions within the plasma. While there are microwave absorbers available with superior vacuum properties, they are either prohibitively expensive or contain ferromagnetic components which may pose a hazard in the large magnetic fields present inside the vacuum vessel.

To gain a sense of the receiving pattern of the antennas we can exploit the

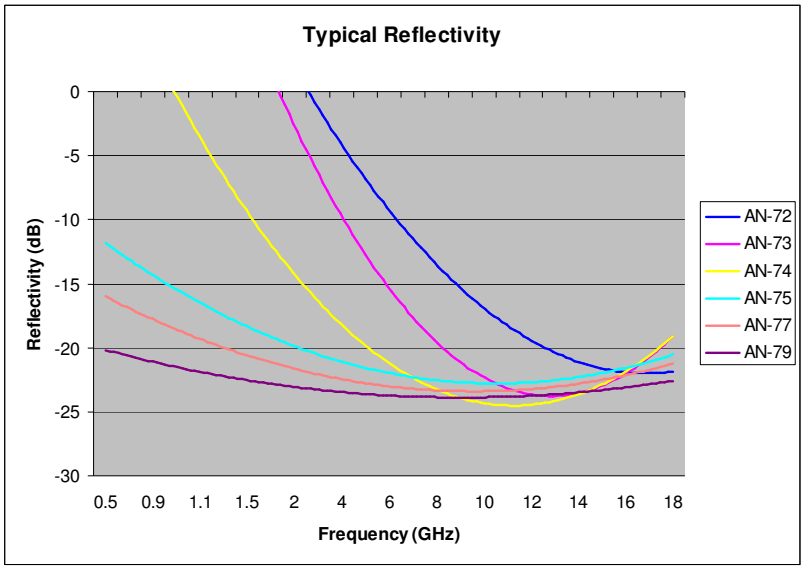

Figure 4.4 – Reflectivity of several thicknesses of standard ECCOSORB®. Reproduced with the permission of Emmerson & Cuming Microwave Products.

symmetry in the the emission and reception of electromagnetic waves. A microwave source is used to send a signal between 30 - 40 GHz out of the ka-band receiving horn. A ka-band detector mounted on a translation stage is then passed through the 10 inch access port in the transition region. The translation stage allows the detector to scan both horizontally and vertically and record the relative intensities of the microwave signal from the horn behind the insulators. Two sample intensity maps are shown in Figure 4.5. The vacuum vessel walls in the mirror throat are lined with ECCOSORB® AN-72 from the jog in the vaccum vessel to a point 20 cm behind the ka-band and X-band horns, see figufe 4.2. The ECCOSORB® does not extend into the transition region because of the proximity with the LGFS and the access port for the turbomolecular pump. If the plasma made contact with the ECCOSORB® there is a possibility that pieces of the ablated material would fall

through the access port and damage the pump.

The finite dimensions of the detector and translation stage prevented measurements from being taken in the full volume, particularly measurements could only be taken within about 1 inch of the core. The vacuum vessel jog from the mirror throat to the transition region spans r =18 - 22 cm. The intensity maps show that, in the absence of plasma, the horns are sensitive to a wide area outside of the rotating plasma volume. The plasma is expected to have a significant effect on the antenna patterns because the overdense plasma acts like a waveguide, forcing waves to travel along the magnetic field lines and essentially focusing the antenna pattern into the plasma. However, even with this assistance the large area covered by the receiving antenna outside of the LGFS suggests that signal contamination remains a concern. The intensity map for 40.0 GHz shows that the beam from the antenna horn is not well collimated at all frequencies. It is not known if the is caused by diffraction in transiting the insulator or by reflections from the walls. In either case, it is clear that isolating the source of the emission from the plasma is not trivial.

4.4 Radial View

In this configuration the horns are mounted at the mid-plane viewing the plasma radially. The horns were mounted on rotatable flanges which allowed the horns to receive incoming radiation with **E** polarized either perpendicular or parallel to the mid-plane magnetic field. The horn antennas are made of aluminium and could easily be damaged by direct exposure to the plasma or by conducting large

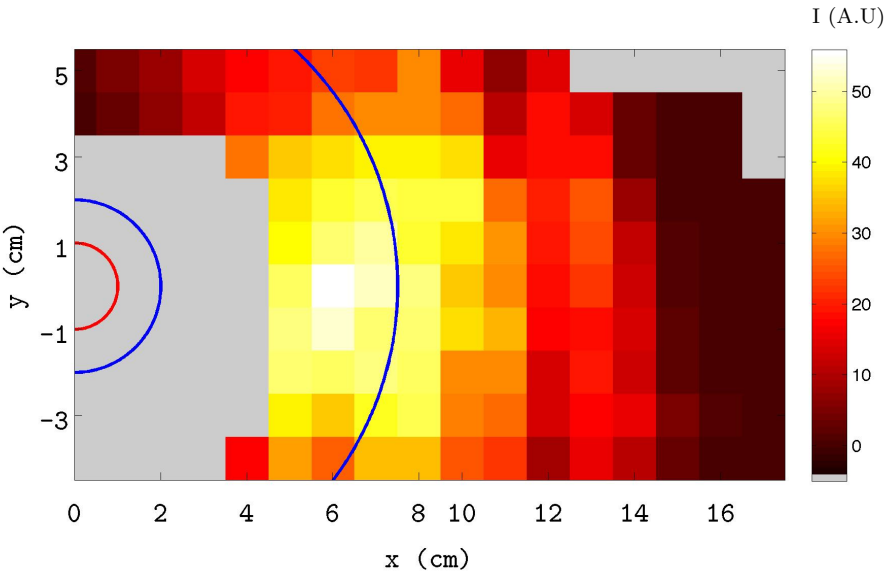

(a)

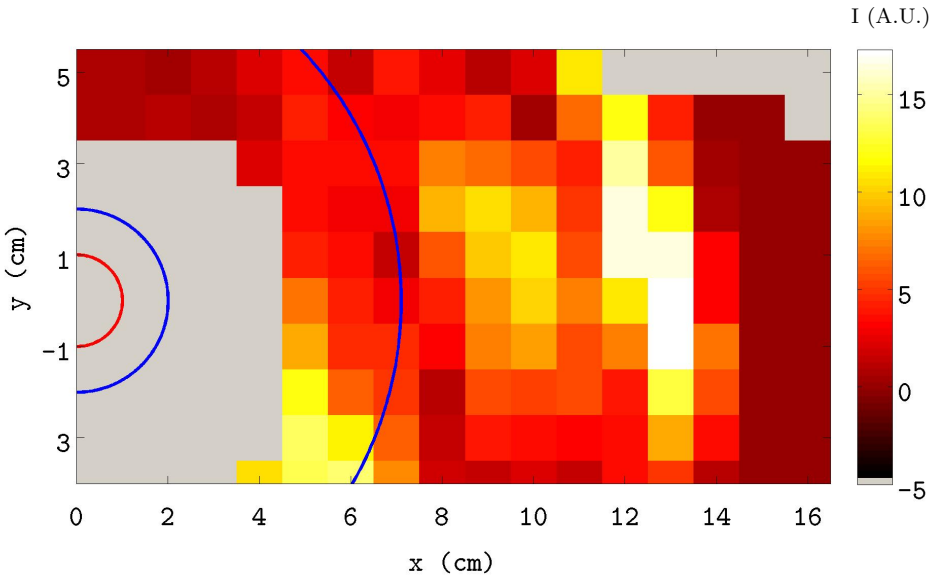

(b)

Figure 4.5 – Axial intensity maps for the ka band horn found at z = 60 cm for 30.0 GHz (a) and 40.0 Ghz(b). Grey corresponds to regions that were inaccessible to the detector. The location of the core is shown with the red circle. The inner and outer LGFS are shown with the blue circles for a mirror ratio of 8.0

electrical currents. To protect them from the plasma the horns are recessed 1 cm behind the main vessel. This places the horns within 2 cm of the rotating plasma and should reduce the impact of reflections and ensure that the horn's viewing angles are essentially filled with plasma.

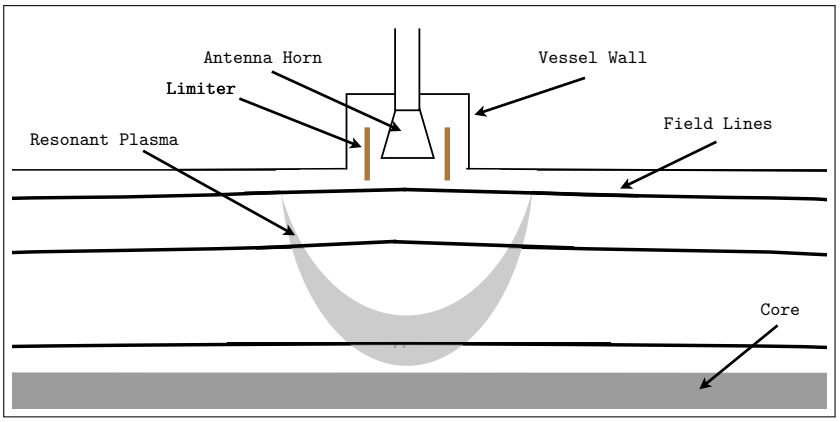

Figure 4.6 – Antenna horn mounted to view the plasma radially and measure X-mode emission shown with the ceramic limiter.

4.5 Local Limiter and Langmuir Probes

In an effort to improve the mode conversion between the Bernstein wave and the X-mode a local plasma limiter was installed to steepen the density gradient and enhance the conversion efficiency. The limiter consists of a tube of fired alumina 7 cm long with an inner radius of 6.5 cm and an outer radius of 7.0 cm. The tube is suspended coaxially with the X-band horn, extending significantly farther toward the plasma than the horn. Because the alumina is difficult to machine the tube is held in place relative to the horn using TorrSeal, which is a durable adhesive that does not outgas significantly in vacuum, to attach the alumina tube to four brass

rods connected to vacuum vessel. The TorrSeal is applied on the inner face of the alumina to limit the exposure of the TorrSeal to the plasma. This arrangement was chosen both for ease of construction and because all of the materials were already available in the lab. The disadvantage is that the configuration is time consuming to change, the entire arrangement must be removed from the vacuum vessel and the old TorrSeal most be removed, the length of the rods changed and the alumina tube reinstalled with fresh TorrSeal.

Because modifying the radial extent of the limiter is time consuming, it is desirable to have a simpler means to vary the penetration depth of the limiter into the plasma. In order to quickly check the extent to which the limiter impacts the plasma and emission characteristics, the strength of the mid-plane magnetic field can be varied while holding the magnetic field in the mirror throats constant. This allows us to vary the radial location of the LGFS anywhere from flush with the vacuum vessel wall to several centimeters away. It should be noted that this changes the mirror ratio, and thus a direct comparison is impossible because the plasma performance is dependent on the mirror ratio.

Three double-tipped langmuir probes are attached to the alumina and measure the density gradient in front of the receiving horn. The radial location of the probe array is fixed relative to the limiter, and the array is aligned to prevent the probes from shadowing each other in the supersonic flows expected inside the LGFS. Each probe consists of two tungsten wires insulated from each other and from the vacuum vessel. In each probe one tip is biased 300 volts negative with respect to the other tip. The current flowing between the probe tips is measured using Avago Technologies

Figure 4.7 – The alumina limiter is shown surrounding the X-band horn and langmuir double probes.

ACPL-790 isolation amplifiers. The amplifiers are inexpensive and provide 200 KHz bandwidth, 15 kV/μs common-mode transient immunity and 0.8 kV work isolation voltage. For a detailed discussion of the theory of electrostatic probes, see appendix A.

4.6 x-ray camera

In any experiment measuring electron temperature with microwave emission, it is important to know if there is a superthermal population of very hot electrons ($T_e \gg 1$ keV) which may contaminate the emission. [12] These electrons can be detected by looking for x-ray photons emitted when the superthermal electrons collide with either the vessel walls or with other charged particles in the plasma.

A Princeton Instruments PIXIS-XO soft x-ray camera is installed viewing the plasma radially at mid-plane in order to investigate the population of hot electrons.

The camera is thermoelectrically cooled to a temperature between -40 and -70 C to enable very low noise operation. Lower temperatures are desired, however it was found that thermal conduction from the hydrogen pre-fill limited the ability of the camera to achieve the lowest temperatures. This was especially true in the case of the relatively dense (30 mTorr) pre-fills used for glow discharges, which limited the operating temperature to -45 C. The camera is sensitive to single photons with energies between 3 and 10,000 eV.

The MCX plasma is not fully ionized outside the LGFS and contains carbon and oxygen impurity ions and is thus a very bright source in the UV and visible range. In order to make a measurement of the x-rays with the PIXIS-XO camera, this light must blocked by a filter to avoid saturating, or possibly damaging the camera CCD. The filter used for this work is composed of two thin Ni foils, each .1 μm thick, which effectively block photons below about 300 eV, while allowing a substantial fraction of higher energy photons to pass through, allowing detection of high energy photons.. The transmission properties of the foil were provided by the Center for X-ray Optics and are shown in Figure 4.8. To prevent energetic electrons from striking either the foil or the CCD a strong magnetic field was applied across the the vacuum tube that led from the MCX mid-plane to the camera.

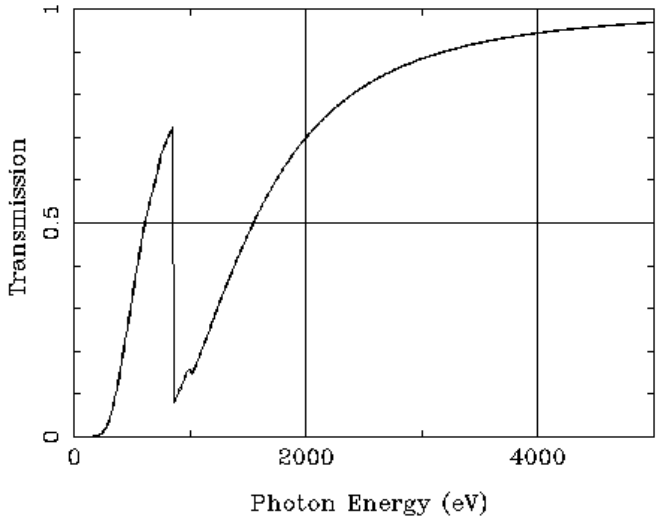

Figure 4.8 – X-ray transmission as a function of photon energy for 0.2 μm of Ni. The filter effectively blocks out UV light from the plasma while allowing substantial transmittance of photons above about 300 eV. Figure courtesy of the Center for X-ray Optics, LLNL

Chapter 5

Theoretical models for microwave emission on MCX

5.1 Overview

Because of the inherent complexity of the equations for wave generation in MCX, any attempt to compare theory against experiment requires numerical calculation of the emission. This chapter will describe the numerical codes developed to make qualitative and quantitative predictions of the microwave emission. Four major codes were created for this purpose. First a 1-D code that calculates the intensity $I(\omega)$ emitted along the axis in the whistler mode. Second, a code which calculates the axial and radial extent of the UHR as a function of frequency and taking density measurements from real MCX discharges as input parameters. Third, a 1-D code which calculates the EBW-X conversion efficiency to estimate the electron temperature based on the detected X-mode emission and plasma density measured at the edge of the rotating plasma. Finally, a 2-D code calculates the theoretical EBW emission spectrum at mid-plane based on the vacuum magnetic field and an assumed radial temperature profile. In all of these programs, the vacuum magnetic field is calculated by treating the external electromagnets as a collection of current loops and solving for the magnetic field given the electric current in the magnet. [27] Predictions for the microwave emission from MCX based on the models will be presented and compared to measured emission in chapter 6.

5.2 Whistler Emission

As shown in Figure 3.1 the whistler mode is able to propagate in the direction of increasing magnetic field, in the case of MCX this is away from mid-plane and toward the ceramic insulators. The cold plasma dispersion relation (3.19) has a singularity at $\omega = \omega_c$ so it is not suitable for calculating the emission intensity. A solution to this difficulty is to use warm plasma theory, which includes the effects from finite larmour radii and removes the singularity in the dispersion relation. This has been done, for example by Stix [19], and the resulting dispersion relation for the whistler mode, neglecting the motion of the ions is

$$\frac{k_\parallel^2 c^2}{\omega^2} = 1 + \frac{\omega_p^2}{\omega k_\parallel}\sqrt{\frac{m}{2\kappa T}} Z\left(\frac{\omega - \omega_c}{k_\parallel}\sqrt{\frac{m}{2\kappa T}}\right) \tag{5.1}$$

This expression can be solved numerically to calculate the absorption coefficient for a given frequency, density and magnetic field. The advantage of (5.1) is that it remains finite at the resonance $\omega = \omega_c$, the disadvantage is that for $\omega > \omega_c$ and $\omega_c \ll \omega_p$ the equation has an infinite number of roots with no way clear way to choose the root that connects to cold plasma solution far from resonance. [16], [28] For numerical calculations the absorption is assumed to be symmetric about the resonance. In practical terms, the absorptivity of the plasmas expected in MCX are high enough that $\tau \gg 2$ is achieved well before the resonance is actually reached, so that the behavior on the far side of the resonance, where the absorption coefficient is uncertain, is unimportant. To calculate the emission from a plasma slab of uniform density and temperature, equation (5.1) is solved for complex wave number k for

a given ω and the absorption coefficient $\alpha = -2\,\mathrm{Im}(k)$. Because the plasma slab is uniform the optical depth is given simply by $\alpha \times l$ where l is the width of the slab. To find the net emission from a series of slabs, the optical depth of each slab is calculated separately, then the intensity emerging from the the first slab is,

$$I(\omega) = B(\omega, T_1)(1 - e^{\tau_1}) + B(\omega, T_2)(1 - e^{\tau_1})(1 - e^{\tau_2}) + ... \tag{5.2}$$

Here we are implicitly assuming that the index of refraction varies slowly enough between slabs that reflections can be ignored. MCX is then modeled as a series of plasma slabs, infinite in r and θ with a width of 1 cm in z. Each slab is assigned a plasma density and temperature. The axial density profile is assumed to be exponential, and is adjusted to fit the density ratios measured by the interferometers at mid-plane and the transition region. The electron temperature is not expected to vary significantly along the length of plasma, so a uniform electron temperature is assumed. The peak density and rate of axial decay are taken from interferometer measurements of a real discharge and the theoretical emission is compared to the measured microwave emission.

5.3 Upper Hybrid Contamination

Signals received when the antenna horns viewed the plasma along the axis showed a spectrum that includes frequencies above the highest cyclotron resonance anywhere in the plasma. Relativistic harmonic generation can be ruled out as the electrons are too cold to generate significant emission in even the second harmonic.

[13] The anomalous emission was seen to disappear when the plasma density dropped to very low values, on the order of $10^{19}m^{-3}$ at mid-plane. Previous work in whistler emission diagnostics for mirrors observed anomalous signals that contaminated the whistler signal and made analysis impossible. [29] In that experiment the emission was eventually attributed to electron Bernstein waves generated by a population of hot electron mode converting to the X-mode at the UHR and reaching the axial antenna after multiple reflections.

In order to investigate the possibility that the anomalous signals originate at the UHR, a matlab script was developed that calculates the extent of the UHR for a given frequency during the discharge. The code partitions the interior of the vacuum vessel onto a rectangular grid. Based on MHD simulations of a centrifugally confined plasma similar to MCX [2] the plasma density is expected to decay exponentially along the magnetic field lines and to be roughly parabolic between the inner and outer LGFS. The plasma density is calculated by assuming a peak value at mid-plane, half-way between the core and the vessel wall. The magnetic field is assumed to be the unperturbed vacuum field. With the density and magnetic field assigned, the code calculates all locations where the Upper Hybrid Resonance condition is met. Figure 5.1 shows the results for mirror ratio 8 over a range of densities for 35.0 GHz. At the typical MCX density, 5 x $10^{20}m^{-3}$ the UHR extends nearly to the insulators, encompassing essentially the entire plasm. As the density is lowered the UHR retreats toward the center of the plasma, eventually vanishing entirely.

This code can be combined with real density measurements to estimate the potential for EBW contamination of the whistler mode. However, estimating the

density for these simulations is a challenge because the suspected EBW contamination only disappears when the peak density is around $10^{-19}/m^{-3}$ which is at the noise floor for the interferometers. With no direct measurement of the plasma density available, the DMLs are used a proxy diagnostic. The peak density during a given shot is determined by the mid-plane interferometer, which is often above the noise floor at the peak density even for very low density discharges. As the discharge progresses and density declines beyond the interferometers capabilities, the DMLs are used to scale the density. This density estimation can then be used to estimate the extent of UHR during the discharge. The accuracy of this proxy method was verified by comparing interferometric results to DML results for normal density discharges ($n \sim 5$ x 10^{20}) and was found to accurately predict the density to within 15%. We assume that the degree of EBW contamination is roughly proportional to the surface area of the UHR and combine the output of this simulation with the expected whistler emission described above. The results of these simulations will be compared with measured signals in Chapter 6.

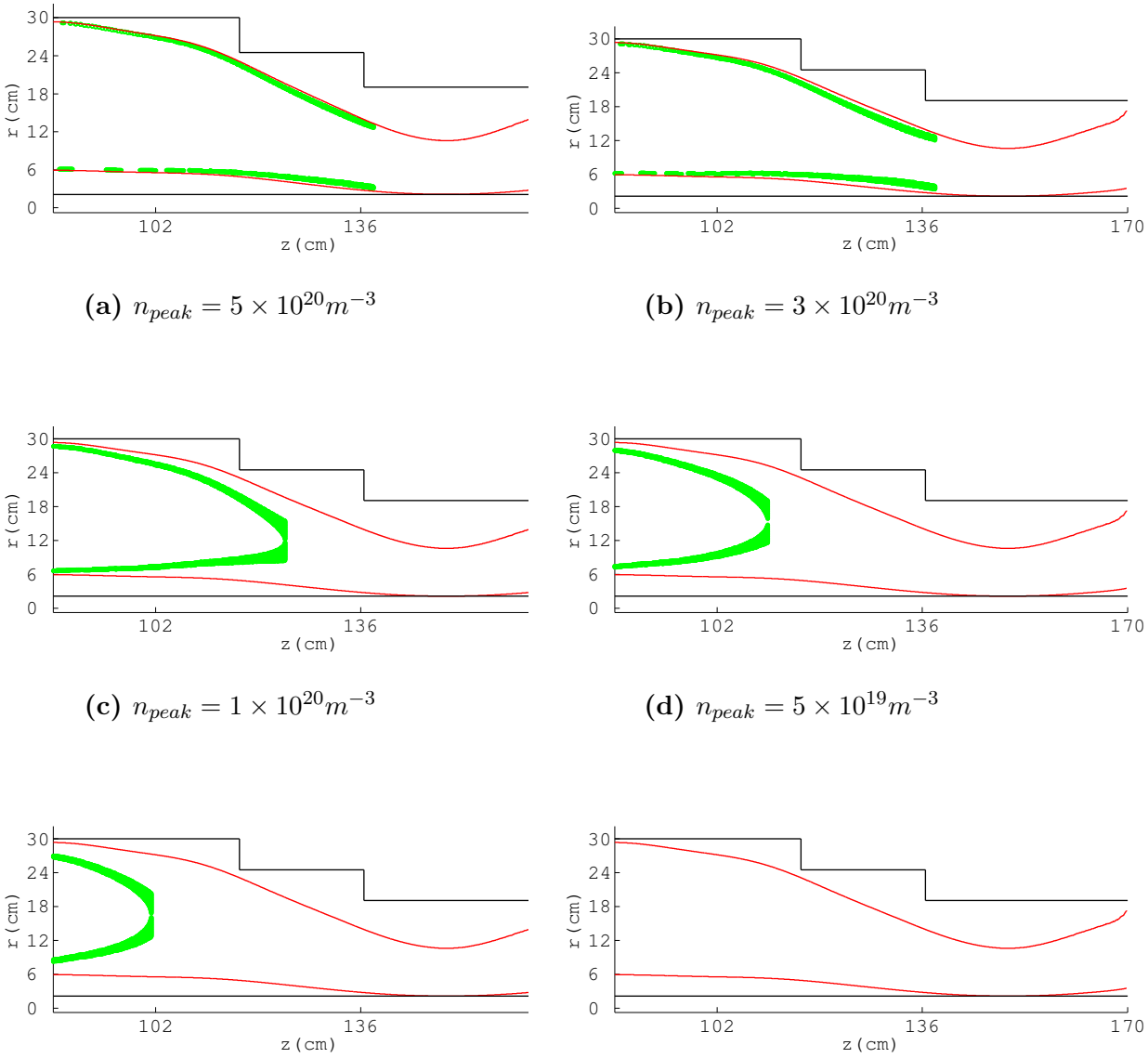

(a) $n_{peak} = 5 \times 10^{20} m^{-3}$

(b) $n_{peak} = 3 \times 10^{20} m^{-3}$

(c) $n_{peak} = 1 \times 10^{20} m^{-3}$

(d) $n_{peak} = 5 \times 10^{19} m^{-3}$

(e) $n_{peak} = 3 \times 10^{19} m^{-3}$

(f) $n_{peak} = 1 \times 10^{19} m^{-3}$

Figure 5.1 – Spatial extent of the UHR layer for $f = 35.0$GHz for several peak plasma densities. As the density falls the UHR layer is seen to retreat towards the center of the plasma and finally vanish for $n_{peak} = 1 \times 10^{19} m^{-3}$

5.4 Electron Bernstein Coupling

A 1-D model has been developed to estimate the coupling efficiency between the EBW and the X-mode on MCX. The model assumes a density profile, scaled to give the same line-averaged density as that measured by the interferometers. The cyclotron frequency $\omega_c(r)$ is calculated using the vacuum magnetic field. For given frequency f the code takes the given density and magnetic profiles to find the UHR and evaluate L_n and α and uses (3.31) to calculate C.

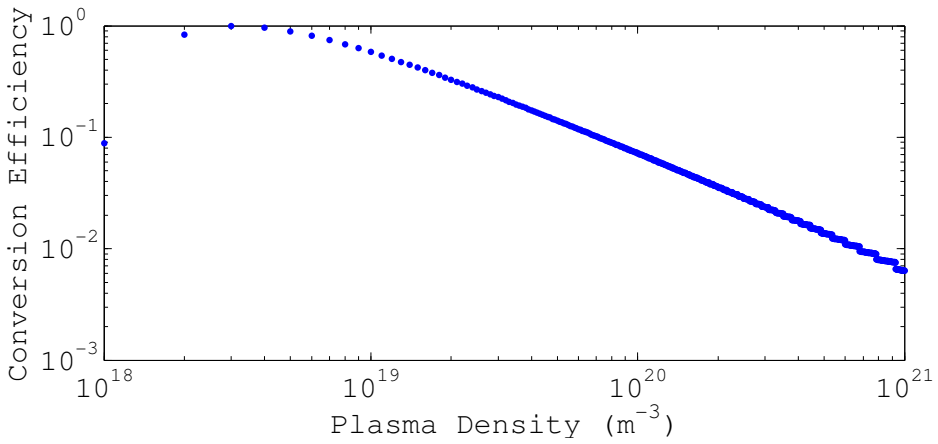

Figure 5.2 – B-X conversion efficiency for $f = 11.6$ GHz as a function of line-averaged density for a parabolic density profile.

The unperturbed density profile on MCX is expected to be parabolic, [2] spanning the radial distance between the inner and outermost rotating flux surfaces. The vacuum magnetic field is not quite uniform, increasing radially toward the center of the vacuum vessel. The 1-D model predicts that the mode conversion efficiency for the 2nd cyclotron harmonic at mid-plane will be less than 1% for the densities that normally occur in the MCX discharge. See figure 5.2. MCX may be operated

with line-averaged densities as low as a few $10^{19}m^{-3}$. However, below this density the capacitor voltage is not sufficient to breakdown the neutral hydrogen to initiate a discharge and at these low densities several standard diagnostics fail. In particular, the spectrometer and interferometer do not have sufficient signal strength at these densities to make any meaningful measurements, limiting our ability to make quantitative comparisons between EBW theory and experiment. Additionally, at this low density significant portions of the plasma become underdense and reflected signals become a problem. The conversion efficiency is predicted to be greater, as much as 20%, away from mid-plane, however these regions are less appealing for diagnostic purposes for two reasons. First the LGFS is at an angle to the access ports, complicating the antenna installation. Second in the transition region the plasma is several centimeters removed from the vessel wall, which increases the role of reflections.

5.5 EBW spectrum prediction

The magnetic field in MCX is spatially inhomogeneous in both the radial and axial directions. The dominant variance is in the axial direction, with the field increasing towards the mirror throats. The magnetic field strength also decreases radially by approximately 12% from it's peak value at $r = 0$ as shown in figure 5.3. For any given frequency f, all plasma along the contour $f = 2f_c$ will be in resonance with the detector and may contribute to the detected emission. The emitted power at a frequency f is thus proportional to the average electron temperature of the

plasma that is in resonance with f.

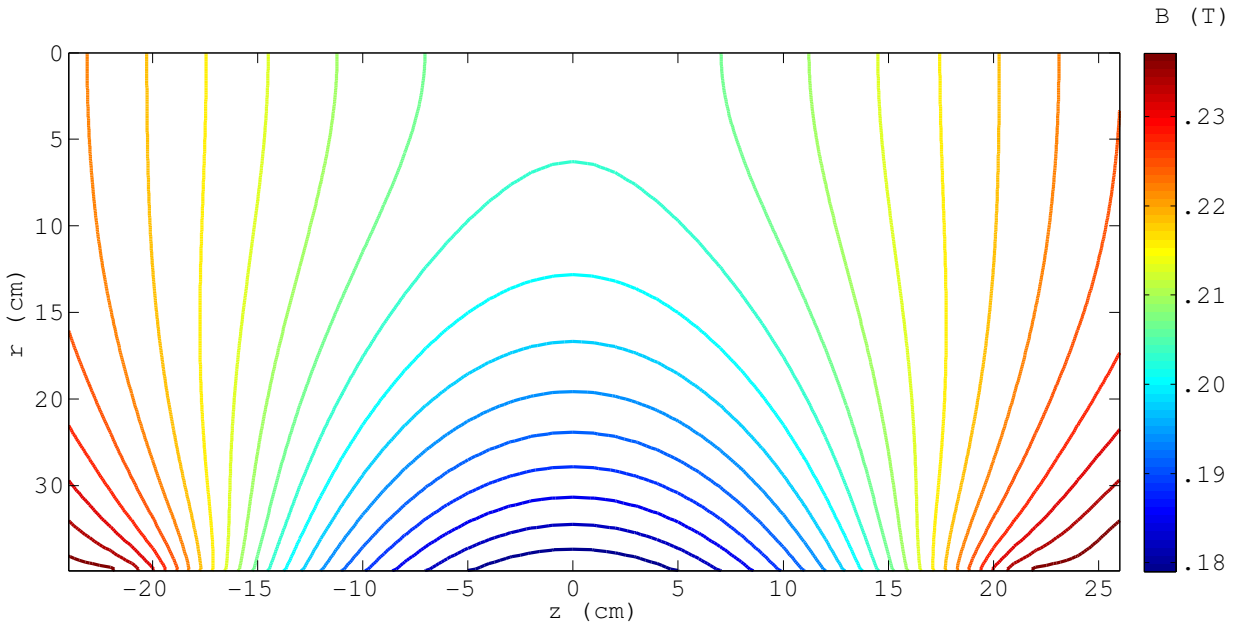

Figure 5.3 – Contour lines of the vacuum magnetic field around the mid-plane of the MCX vessel. $r = 0$ corresponds to the axis of rotation.

The model used to predict the emission spectrum uses the vacuum magnetic field to calculate the surface area of the resonant zone that is accessible to the antenna horn's view and calculates the emission based on an assumed electron temperature profile. The code works on a rectangular region spanning $0 \leq r \leq 30$ cm and $-50 \leq z \leq 50$ cm. This region is then divided into a mesh of grid points, each with an electron temperature and cyclotron frequency determined by the vacuum magnetic field and an assumed electron temperature profile. The entire volume of resonant plasma is not accessible to the horn as EBWs propagate primarily perpendicularly to the local magnetic field. Numerical ray tracing calculations done using the full warm plasma dielectric tensor performed on CDX-U, a plasma with similar

plasma parameters and magnetic curvature to MCX show that a spread of about 15 - 20 degrees may be expected. [25] To account for this, the code excludes the plasma outside of a cone with an angle that may be defined between 0 and 90 degrees. Typical calculations use a range from 10-50 degrees. The electron temperature profile is assumed to be skewed parabolic. The skewed profile is calculated using:

$$T_e(r) = T_0\left(ar^2 + 1\right)\left(1 + \mathrm{erf}\left(\frac{sr}{\sqrt{2}}\right)\right) \tag{5.3}$$

where a is chosen to enforce $T_e = 0$ at the LGFSs, T_0 is the peak temperature and s is a skew parameter. The code assumes that the resonant zones are optically thick. Information on the electron temperature profile and angular spread of EBW propagation may be found by calculating the emission spectrum over a range of test profiles and spreads and seeking the conditions that best match experimental results.

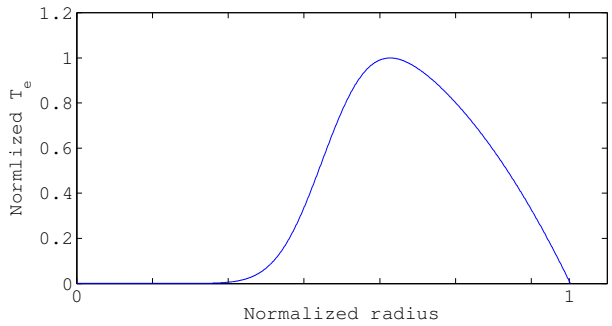

(a) s = 5

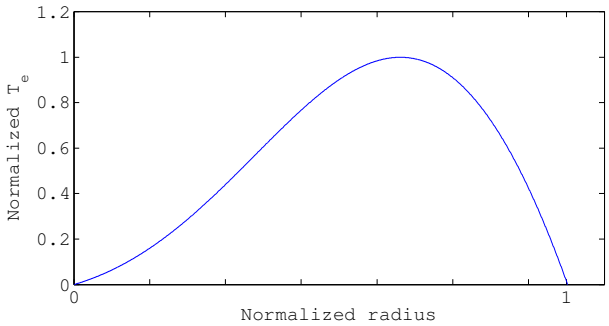

(b) s = 1

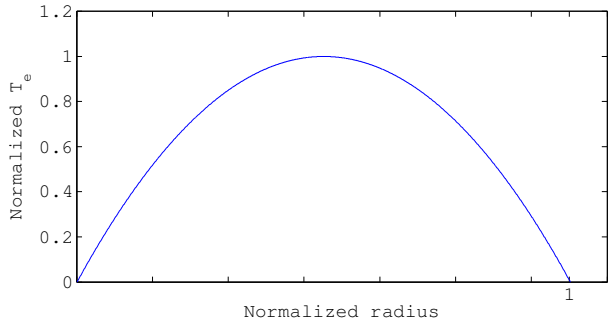

(c) s = 0

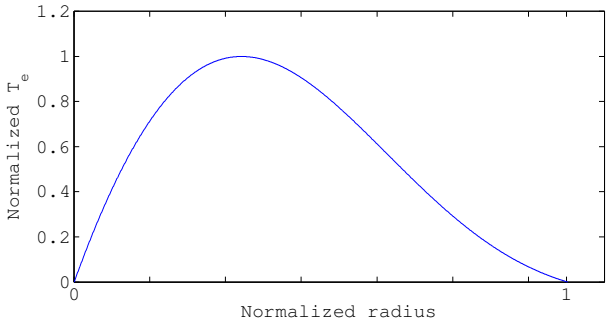

(d) s = -1

Figure 5.4 – A selection of possible electron temperature profiles with skew parameters ranging from 5 to -1. The radius is normalized to $r = 0$ and $r = 1$ and the inner and outermost rotating flux surfaces.

Chapter 6

Experimental Results and Analysis

6.1 Introduction

In this chapter we show the experimental observations connected with our effort to measure the electron temperature in the MCX plasma. First, we present the measurements taken with the X-ray camera which show that no detectable X-ray emission is generated by the rotating plasma. Measurements of axial emission are presented and compared with theoretical modeling. Next, we present results gathered by looking at emission in the X- and O-modes at mid-plane. The emission is shown to be consistent with mode-converted EBWs and the wave intensity is used to estimate the radial electron temperature profile. Finally, we show that the measured electron temperature is in reasonable agreement with a temperature estimation based on energy balance between electron-ion collisional heating and heat loss from electron recycling at the insulators. Where error bars are presented, they represent 1 standard deviation from the mean unless otherwise noted.

6.2 X-rays and hot electrons

Before discussing the results of the microwave emission studies, we first establish that the MCX plasma does not contain a substantial population of hot electrons

($T_e > 1$keV). Because a large voltage difference exists across the MCX plasma, there is a significant possibility that the plasma contains a superthermal population of hot electrons with energies on the order of the discharge voltage. These electrons would contaminate the microwave emission from the plasma and complicate the analysis of the received signals. [13]

In order to verify the x-ray camera's operation a glow discharge plasma expected to emit detectable x-rays was established in the MCX vacuum vessel. First the chamber is filled with hydrogen to a pressure of 30 mTorr. A high voltage is applied to the core to break down the gas and form a plasma. There is no magnetic field in this case, so some electrons are expected to achieve energies on the order of the potential between the core and the vacuum vessel. When these electrons collide with other particles, or with the vessel wall they will generate photons with kV energies. The glow discharges can be maintained in steady state anywhere from 1-6 keV indefinitely, which allows good statistics to be gathered. For each discharge voltage, 300 camera exposures were taken. Each exposure is 10 μs long. A sample of one exposure is shown in Figure. 6.1

The "spots" in Figure 6.1 are caused by individual photons striking the CCD. Higher energy photons induce stronger signals, up to saturation of the CCD pixel. By using several different glow discharge voltages, a rough idea of the correspondence between the degree of pixel saturation and photon energy can be established. For every exposure taken, each pixel is classified according to percent saturation, rounding to the nearest 5 percent and the total number of pixels in each bin is calculated. This number is then averaged over 300 exposures. The results are shown in

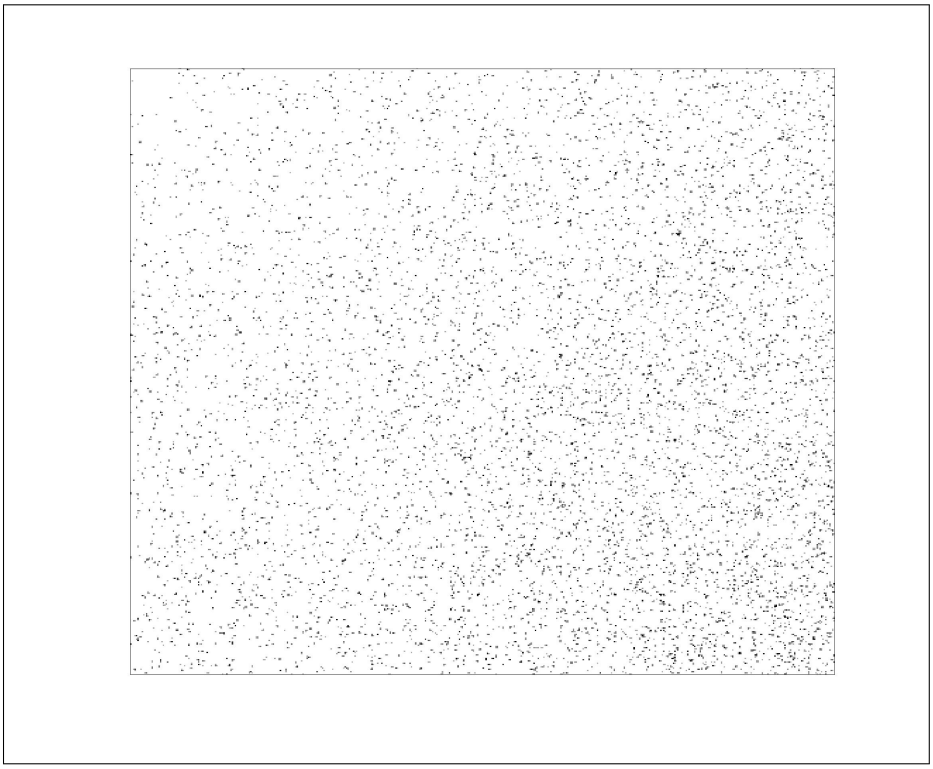

Figure 6.1 – A 500 x 500 pixel sample from an image taken using a 3.0 kV hydrogen glow discharge. Darker spots correspond to greater saturation on the CCD.

Figure 6.2. Clearly higher glow discharge voltages generate higher energy photons.

Having established confidence in the operation of the x-ray camera through the glow discharge analysis, we can investigate the production of hot electrons in the rotating plasma. A series of 300, 1ms "background" exposures was taken with a 5 mTorr pre-fill of hydrogen gas in the chamber, but with no plasma or magnetic field in order to establish a baseline for the plasma exposures.. Next a series of 69 normal MCX shots was run with the x-ray camera exposed from 1.5 - 2.5 ms after breakdown. The binning analysis described above was done for the baseline and the plasma exposures. The comparison of the plasma exposures with the background is

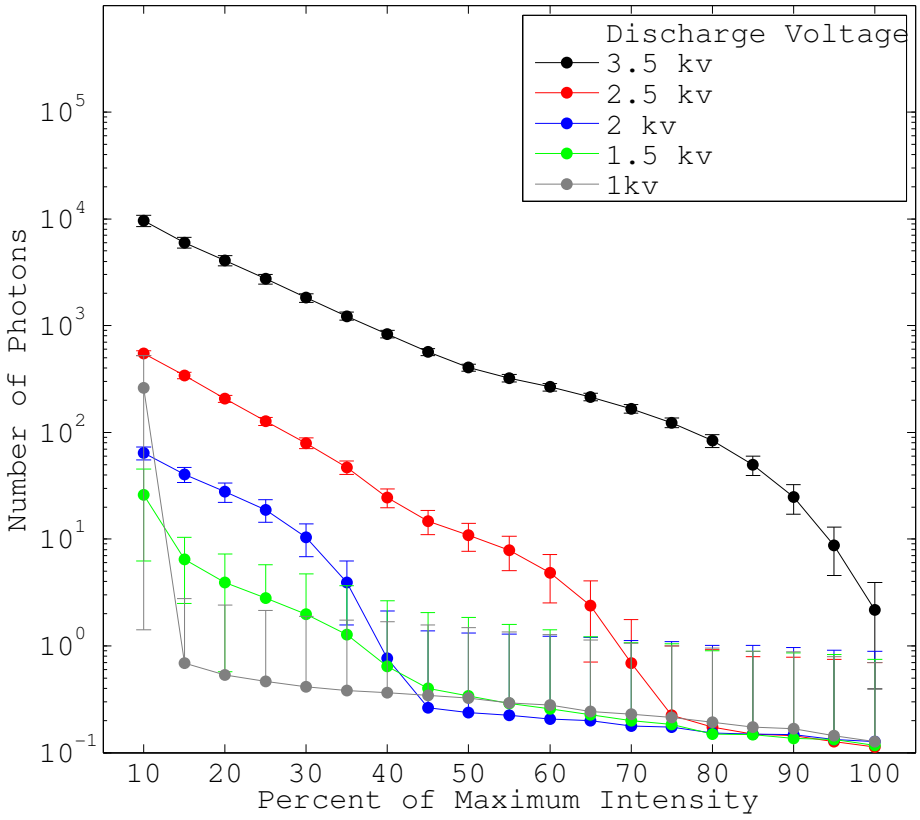

Figure 6.2 – Distribution of percent pixel saturation for several glow discharge voltages.

shown in Figure 6.3. The x-ray emission from the rotating plasma is virtually indistinguishable from background. Comparing this result with the data from the glow discharge measurement we conclude that within current measurement capabilities there are no electrons in the MCX plasma with energies greater than 1 keV.

Because of thermal noise in the camera, it cannot be used to rule out the possibility of electrons with energies below 1 keV but still substantially hotter than the thermal electrons. Such electrons will suffer collisions with the cold background electrons and eventually thermalize, so it is natural to ask how long a 1 keV electron

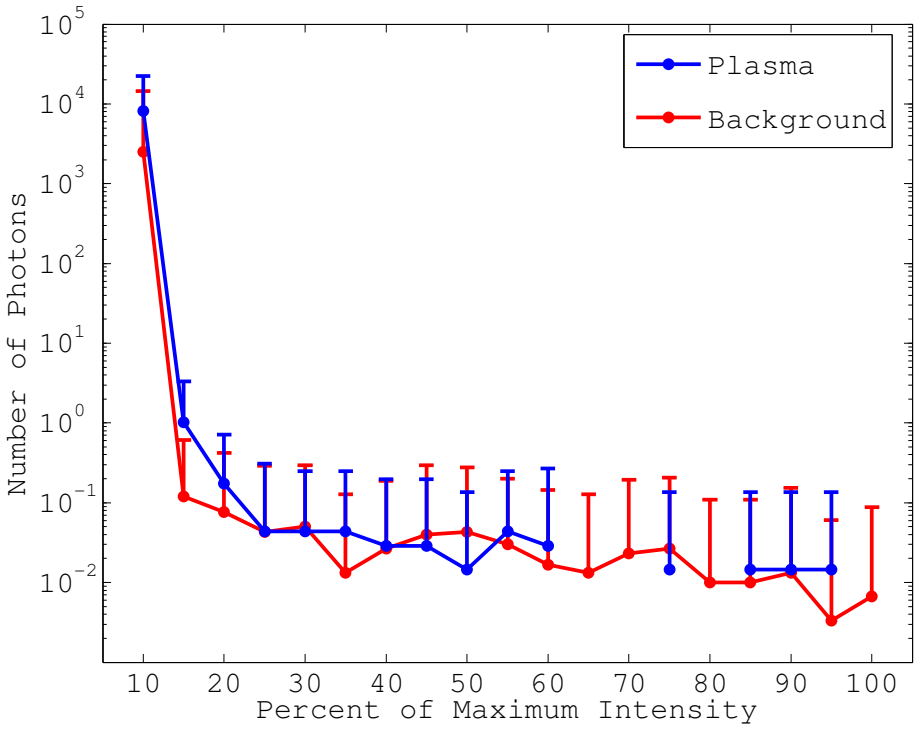

Figure 6.3 – Distribution of percent pixel saturation for several glow discharge voltages.

will take to thermalize with the MCX plasma. Estimations for how long electrons with this energy would persist before thermalizing with the bulk plasma can be made using the standard equations for the slowing down time. [30]

$$\frac{d\mathbf{v}_\alpha}{dt} = -\nu_s^{\alpha\backslash\beta}\mathbf{v}_\alpha \tag{6.1}$$

$$\nu_s^{\alpha\backslash\beta} = (1 + m_\alpha/m_\beta)\,\psi\left(x^{\alpha\backslash\beta}\right)\nu_0^{\alpha\backslash\beta} \tag{6.2}$$

$$\nu_0^{\alpha\backslash\beta} = \frac{4\pi e_\alpha^2 e_\beta^2 \lambda_{\alpha\beta} n_\beta}{m_\alpha^2 v_\alpha^3} \tag{6.3}$$

$$\psi(x) = \frac{2}{\sqrt{\pi}} \int_0^x t^{1/2} e^{-t} dt \tag{6.4}$$

$$x^{\alpha\backslash\beta} = \frac{m_\beta v_\alpha^2}{2kT_\beta} \tag{6.5}$$

Numerical solution of (6.1) show that a 1 keV electron will thermalize with a background plasma of $5 \times 10^{20} m^{-3}$ density and 100 eV temperature in about 0.1 μs. Microwaves with frequencies corresponding to the core of the rotating plasma are observed in burst of emission lasting 10s of μs, which is much longer than the thermalization time. Thus we conclude that it is unlikely that the observed emission contains superthermal contributions from hot electrons.

6.3 Axial Emission

In this section we will examine the radiation detected with the horn antennas looking axially through the ceramic insulators. This radiation was found to have an emission spectrum that cannot be explained completely by whistler mode emission and was ultimately abandoned for diagnostic purposes because it was not possible to identify positively where in the plasma the radiation was emitted under normal discharge conditions. After examining the emission in some detail we conclude that the observed microwaves consist of electron cyclotron emission in the whistler mode contaminated by emission from elsewhere in the plasma. The most likely candidate for the contaminating emission is mode converted EBWs from the UHR arriving at the axial horns after several reflections.

The axial view is expected to measure primarily radiation that originates in the overdense region of the plasma that then propagates axially away from the mid-plane, mode converting to circularly polarized microwaves at the interface of the plasma with the insulator. This radiation should exhibit two key features, it should not be sensitive to the polarization of receiving horn, and it should only be present in frequencies that satisfy $\omega = \omega_c$ for some region on the plasma. For this reason early work focused on the Ka-band frequencies, because it is possible to operate MCX at low enough magnetic fields to exclude frequencies above 28 GHz in order to determine whether or not the emission originates from a cyclotron resonance.

The axial emission spectrum from 30-40 GHz was measured by averaging the emission from 1.5-2.5 ms after the initial plasma breakdown. In the first series of discharges, shown in figure 6.4a, a cyclotron resonance exists in the plasma for the entire frequency band and ECE emission in the whistler mode is expected. In the second series, shown in figure 6.4b the peak cyclotron resonance occurs at 35.1 GHz, and emission above this level is not expected, however emission is observed above the peak cyclotron frequency at intensities similar to the intensities below the peak cyclotron frequency. This demonstrates clearly that the whistler mode signal is being contaminated by emission from some other source in the plasma.

Various experiments with dense magnetized plasma columns have reported the generation of microwave emission near the harmonics of the cyclotron frequency in plasmas much too cold for relativistic effects to be important. [31] [32] [33] [29] In some cases up to the 25th harmonic could be observed. [31] Mode-converted EBWs emerged as a possible explanation for the high harmonic emissions. [34] In the case

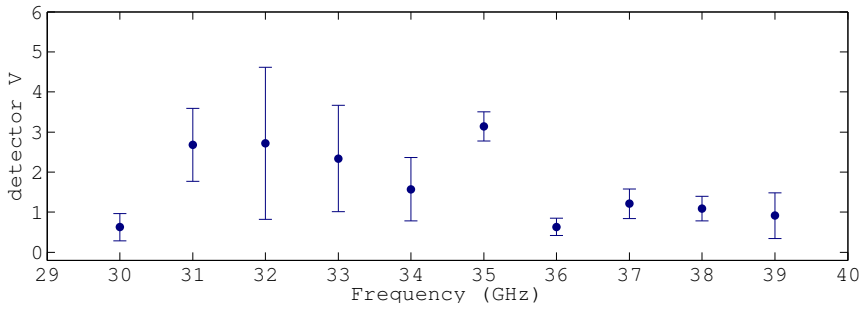

(a) $B_{mid} = 0.212T$, MR = 8.0

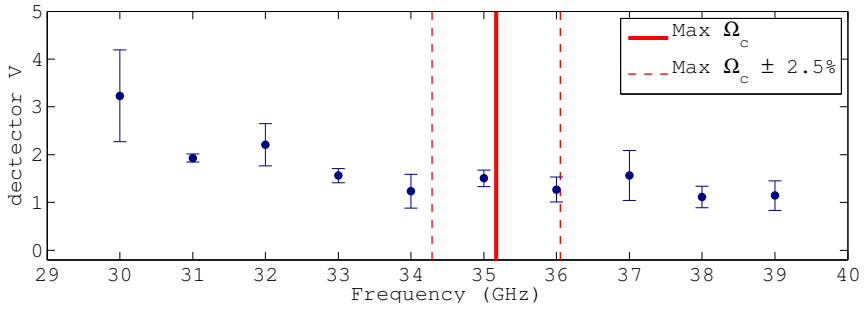

(b) $B_{mid} = 0.159T$, MR = 8.0

Figure 6.4 – Average axial emission averaged over 1.5-2.5 ms after the plasma breakdown. (a) The peak cyclotron resonance in the device is above 40 GHz. (b) The peak cyclotron resonance occurs just above 35 GHz.

of [29], the emission was shown conclusively to originate at the UHR layer and to originate with a population of hot (200 eV) electrons from a cathode discharge used to ionize the the background plasmas. Because MCX operates at very high densities ($\omega_p \sim 10\omega_c$) a UHR layer surrounds the plasma for all $f = 2f_c$ giving mode-converted EBWs a possible exit from the plasma across a very broad range of frequencies. See figure 5.1. The UHR for a particular frequency can only be removed by lowering the plasma density until the condition $\omega = \sqrt{\omega_p^2 + \omega_c^2}$ is no longer met at any point in the plasma.

The density in MCX can be loosely controlled by varying the density of the hydrogen pref-fill, with an available range of 0.5 - 50.0 mTorr. If the pre-fill is moved beyond this range then there are either too many or too few particles in the chamber for the avalanche breakdown to proceed. The plasma density at the lowest possible pre-fill results in plasmas with densities on the order of $10^{19}m^{-3}$, although exact measurements become difficult as these densities are close to the noise floor of the interferometer. As shown in section 5.3 the density in this range can reduce, and in some cases eliminate, the UHR from the plasma. The scheme is only valid at the Ka-band range of frequencies however, as the plasma densities low enough to remove the UHR between 8.2 - 12.4 GHz cannot be sustained in MCX.

To investigate the UHR emission as a possible source of the anomalous emission a series of discharges was run with 0.5 mT hydrogen pre-fill to lower the plasma density. The magnetic field was set so that the maximum cyclotron resonance in the device varied from less than 29.0 GHz to more than 39 GHz. For each field intensity the emission spectrum was built up by changing the Ka-band radiometer frequency from shot to shot. The goal of these discharges was to observe emission from a plasma that initially has high enough densities to contain a UHR and support Bernstein emission, and then evolves to a plasma with insufficient density to contain the UHR. The plasma was terminated by the crowbar ignitron at 8 ms rather than the typical 5 ms. The extra time allowed the plasma density to decay for a longer time as the capacitor bank voltage driving the discharge dropped. The observed emission spectrum depended on the strength of the magnetic field, and also on the time during the discharge the spectrum is measured. The emission spectrum

measured early in the discharge, for six different magnetic field settings, is shown in figure 6.5. Emission is observed at all measured frequencies in every case, although emission at or below the peak cyclotron resonance is generally greater by as much a factor of 2-3. The emission characteristics change at later times, as shown in figure 6.6, emission above the peak cyclotron emission disappears and the spectrum is consistent with whistler emission.

A computer code was developed as described in chapter 5 using Matlab software to combine the predicted whistler emission with an estimate for the contamination from the EBW emission. The code takes the average density $n(t)$ from 40 low density discharges and calculates the extent of the UHR for an "average" discharge. The whistler emission is calculated using the average measured density as an input. A constant, uniform electron temperature is assumed in order to simplify the calculation. The average measured microwave emission between 30 - 40 GHz is plotted in figure 6.7 together with the predicted emission generated by the computer code for the same band.

Early in the discharge, emission is observed at all frequencies, with those below ω_{cmax} generally dominating those above ω_{cmax}. In the latter half of the discharge, the behavior changes dramatically, the emission above ω_{cmax} disappears almost entirely, while emission below ω_{cmax} intensifies steadily until the discharge is terminated. The predicted emission is in good qualitative agreement with observed emission, reproducing both the early dominance of frequencies below the peak cyclotron frequency and the timing of the disappearance of emission above the peak cyclotron resonance. The striking qualitative agreement between the observed and predicted

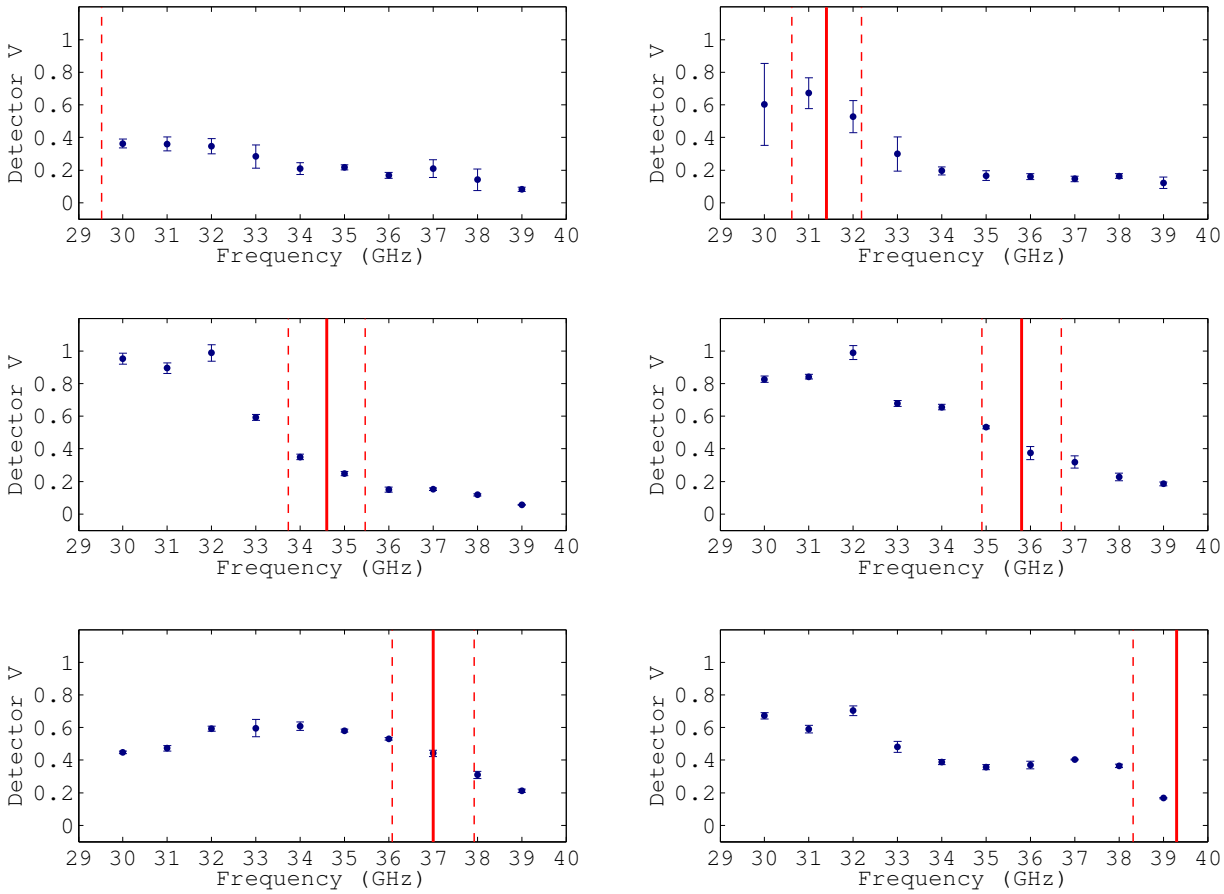

Figure 6.5 – Average detector voltage measured from 1.5 - 1.6 ms after breakdown in the Ka-band looking axially through the ceramic insulators shown as a function of frequency for several overall magnetic field intensities. The solid red line indicates the cyclotron frequency corresponding to the peak magnetic field in the device, located at the mirror throat. The dashed lines indicate the peak field ±2.5%, the accuracy with which the magnetic field strength is known.

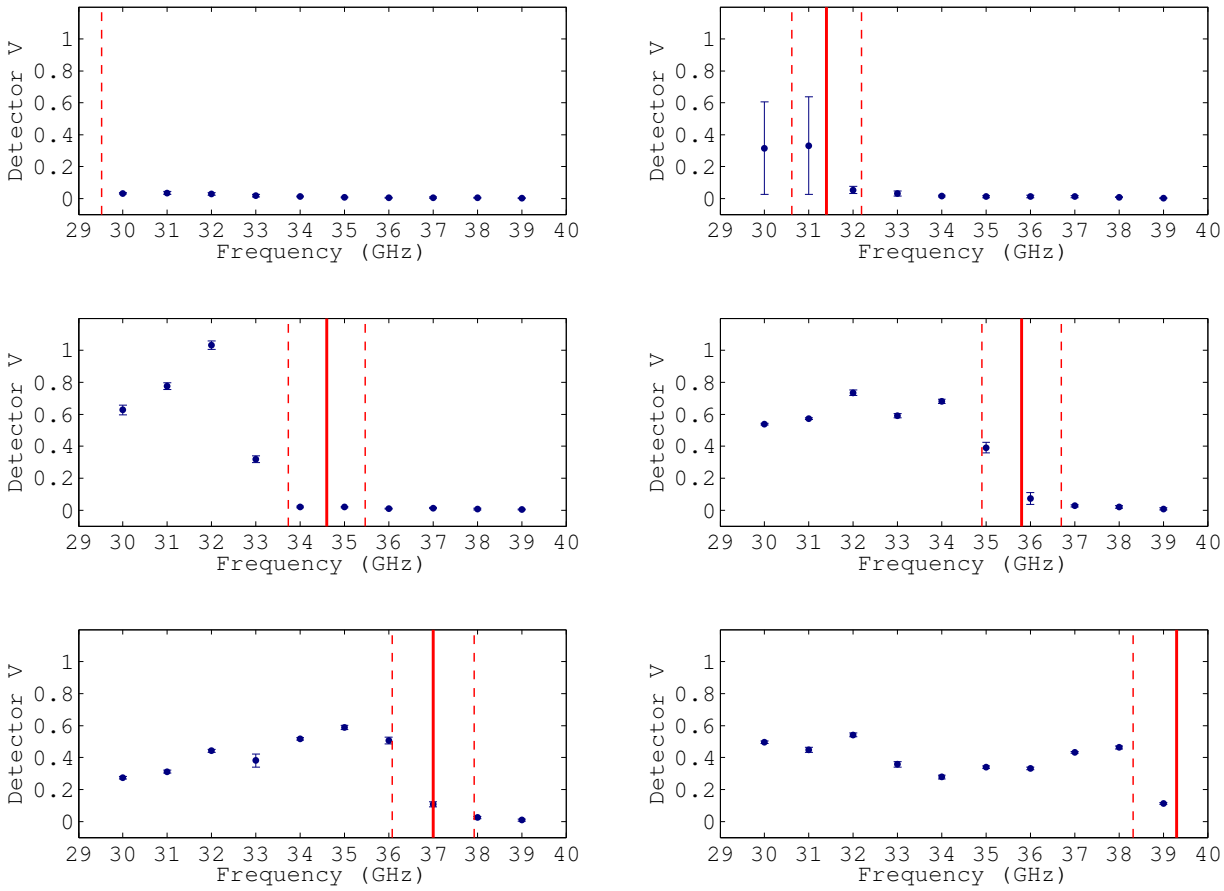

Figure 6.6 – Average detector voltage measured from 6.5 - 6.6 ms after breakdown in the Ka-band looking axially through the ceramic insulators shown as a function of frequency for several overall magnetic field intensities. The solid red line indicates the cyclotron frequency corresponding to the peak magnetic field in the device, located at the mirror throat. The dashed lines indicate the peak field ±2.5%, the accuracy with which the magnetic field strength is known.

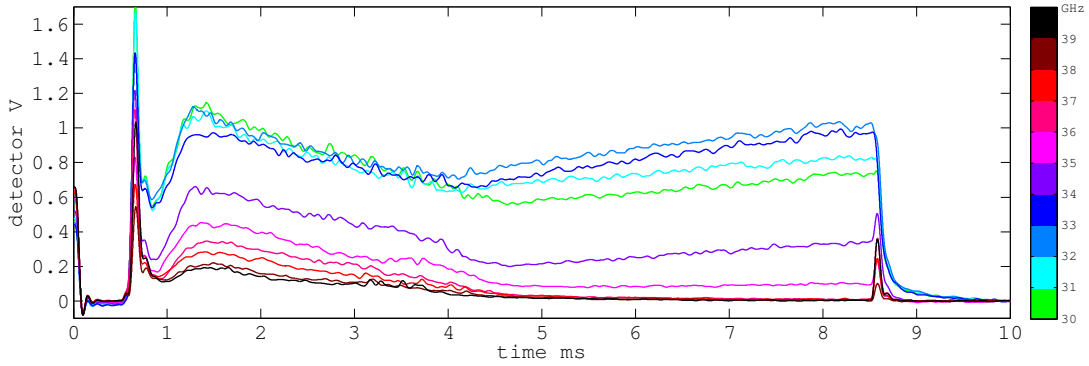

(a) observed emission

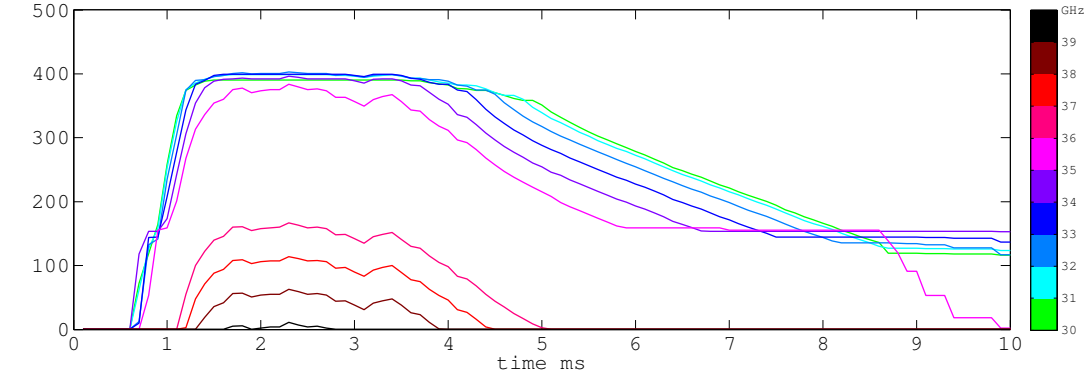

(b) predicted emission

Figure 6.7 – Measured (a) and predicted (b) axial microwave emission in the 30 - 40 GHz range. The maximum cyclotron resonance in the machine for these shots was 34.6 GHz. In (a) the trace for each frequency represent an average over 4 discharges.

emission strongly suggests the EBW emission from the UHR is responsible for the anomalous axial emission.

Concluding that the contaminating emission originates with mode-converted EBWs a microwave absorbing material, ECCOSORB® AN was installed along the vacuum vessel to try and absorb the UHR emission before it could reach the axial antennas. Electron Bernstein waves are strongly damped along magnetic field lines [19] so that propagation is limited to motion across the magnetic field. For this reason we expect that EBW emission cannot reach the axial horns directly, because they look parallel to the magnetic field. As discussed in chapter 4 however, the horn's view contains portions of the reflective vacuum vessel wall so that it is possible that EBWs may escape the plasma perpendicular to the magnetic flux surfaces and reach the axial horns after several reflections from the vessel walls. Only vessel walls in the mirror throat were covered with absorber in order to limit plasma - absorber interactions that could damage the ECCOSORB® and contaminate the vacuum vessel with carbon. This compromise attempted to balance the need to absorb the UHR contamination against the need to protect the vacuum vessel and was ultimately unsuccessful as shown in figure 6.8.

The ECCOSORB® failed to eliminate the contamination from the UHR; the contaminating emission is still within a factor of two of the emission detected in the primary cyclotron band. The tests which concluded that reflected UHR emission was contaminating the Ka-band measurements cannot be duplicated for the X-band because the magnetic field cannot be lowered enough to exclude the X-band frequencies from the device. However, since reflections are known to contaminate

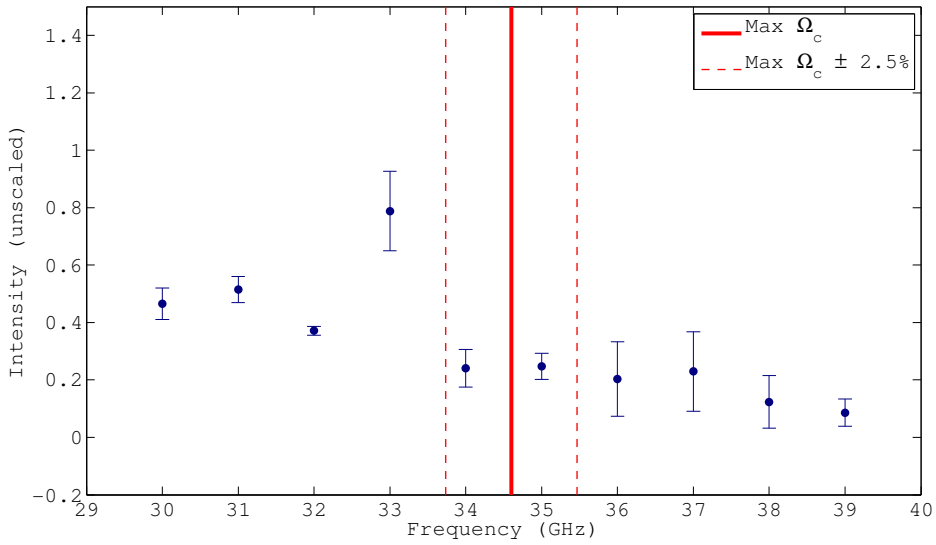

Figure 6.8 – Plasma emission spectrum from 30 - 40 GHz measured after the mirror throat vacuum vessel has been lined with ECCOSORB® microwave absorber. Emission is observed well above the peak cyclotron resonance. Overall emission intensity is also reduced.

the Ka-band signals, it is certainly reasonable to assume that the X-band signals are equally affected. Ultimately, as a result of the difficulty of reflections, and the complications related to transmission through the insulator, the axial view was abandoned as a potential temperature diagnostic.

6.4 Radial View without limiter

The first measurements of the radial emission were made using the X-band horn between 8.2 - 12.4 GHz, a band that contains the 2nd cyclotron harmonic for the plasma at mid-plane with the horn oriented to receive emission in the X-mode. The horn was recessed 2 cm behind the vessel wall to avoid drawing any current

and prevent contact with the plasma which could damage the horn. The frequency of the radiometer was varied shot to shot over this frequency range. The observed emission was mostly flat, with a few large "spikes" in the emission lasting only 1-10 μs. These spikes were initially thought to be noise and several attempts were made to eliminate them.

First, the waveguide used to transmit microwaves from the receiving horn to the radiometer was blocked with a thin sheet of aluminum foil, which eliminated the spikes along with the rest of the signal, ruling out the possibility of stray pickup in the receiver circuitry. Electrostatic coupling to the plasma is unlikely, as the horn is recessed behind the vessel wall and the waveguide is brazed to vacuum vessel. Finally clear evidence was found that the emission spikes originate in the plasma in that the spikes only appear when the horn is oriented to receive emission polarized in the X-mode. As shown in Figure 6.9 the spikes do not appear when the horn is oriented to detect the emission in the O-mode. Additionally the emission spikes are observed only at frequencies that satisfy $\omega = 2\omega_c$ for some region of the plasma, when the radiometer is tuned below these frequencies no spikes in the emission are observed. Since there are always regions of the plasma with $\omega_c > 12.5$ Ghz it was not possible to tune the radiometer above the upper limit of cyclotron frequencies to see if emission occurs in that region.

The emission spikes were found to be correlated with the cyclical crash in the plasma voltage that is a common feature of the MCX discharge. This is shown in Figure 6.10. This provides further confidence that the spikes are real plasma emission rather than noise. The crashes in the plasma voltage are thought to be

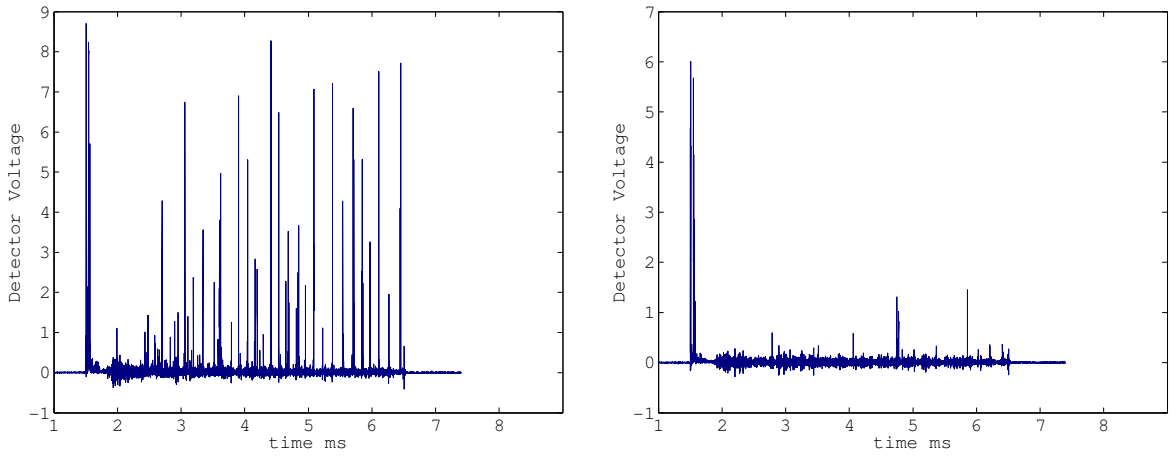

(a) X-mode **(b)** O-mode

Figure 6.9 – Received X- and O-mode emission from two discharges taken under identical experimental conditions without the use of the local limiter. The receiver was tuned to 11.33 GHz in both cases, corresponding to the vacuum magnetic field near the expected peak in plasma density.

the result of an m = 2 interchange mode [7] [9] that is periodically destabilized by the rotation. The interchange leads to turbulent transport of plasma density out of the interior of the plasma and towards the vacuum vessel wall. As the dense plasma is expelled to larger radii conservation of momentum slows the plasma rotation, which stabilizes the interchange and allows the rotation to recover and the cycle repeats. A potential explanation for the emission spikes emerges as follows: EBWs are continuously generated in the core of the plasma at twice the cyclotron frequency and propagate toward the plasma edge, but the density gradient is either too shallow or too steep to allow them to effectively couple to the X-mode and the EBWs are reflected back into the plasma. As the plasma rotation increases, the m

= 2 interchange is destabilized and transports plasma density outward towards the walls, leading to a brief increase in the density gradient and allowing the EBWs to couple to the X-mode.

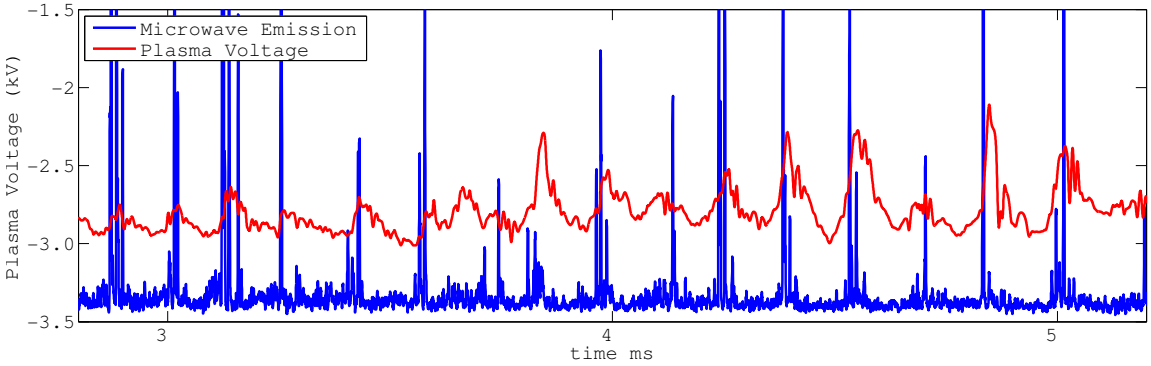

Figure 6.10 – Emission spikes overlaid with the plasma voltage for the same discharge. The plasma voltage is shown in red, X-mode emission is shown in blue. The spikes are seen to occur midway through each crash in the plasma voltage.

The relationship between the plasma voltage and the edge of the rotating plasma can be investigated using the internal ring of magnetic probes. The array of internal magnetic probes measures fluctuations in the magnetic field at edge of the plasma caused by turbulence in the rotating plasma. In figure 6.11 the fluctuations in the magnetic field are shown along with the simultaneous crashes in the plasma voltage; the spatial FFT of the probe signals is also shown to show the mode number of fluctuations up to m=4. The voltage crash is seen to coincide with strong excitation of both the m=0 and m=2 modes. The large m=0 mode during the voltage crash indicates that the plasma expands radially, pushing magnetic flux out toward the vacuum vessel while the plasma voltage, and hence the rotation speed,

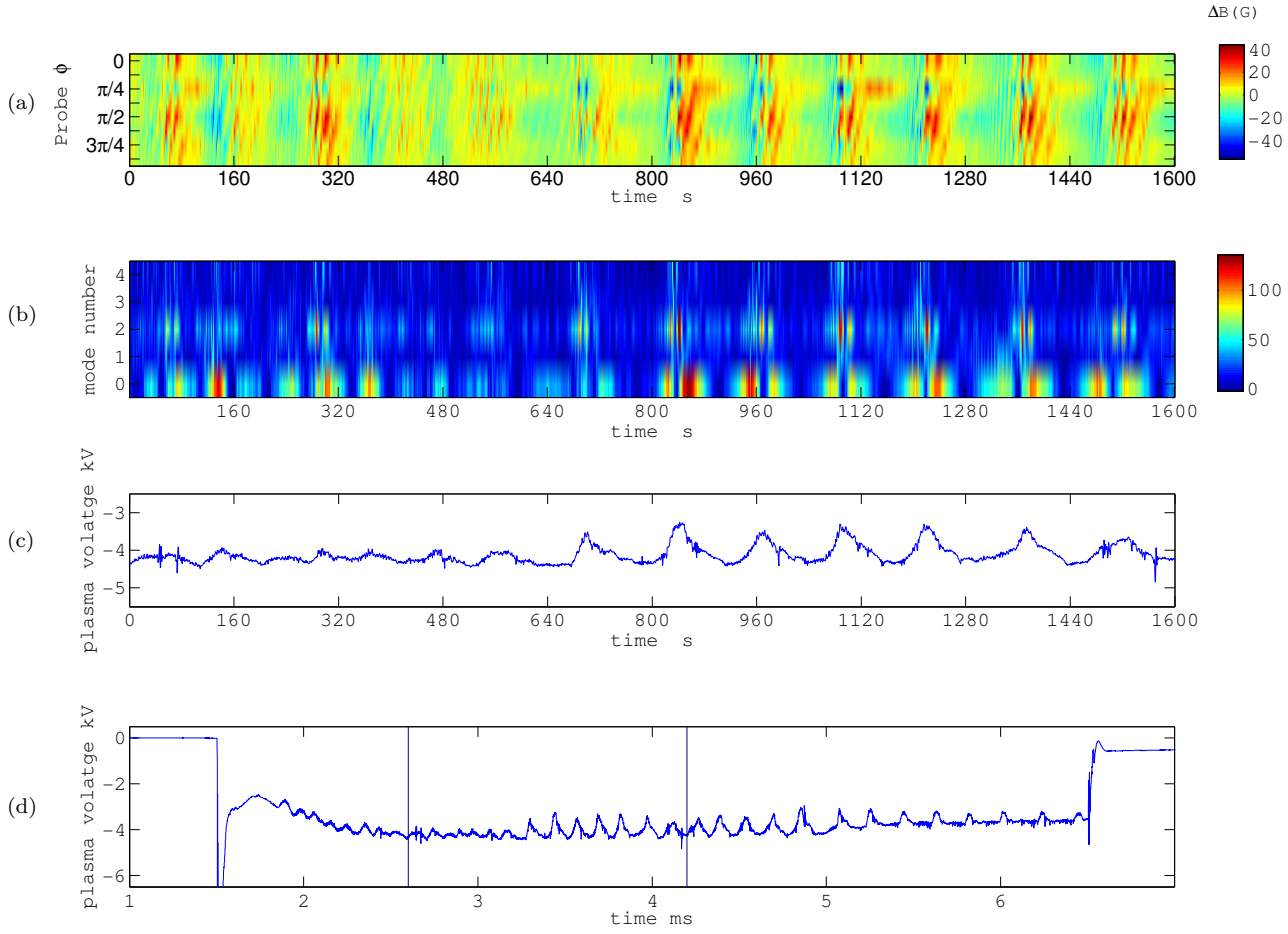

Figure 6.11 – Relationship between the voltage crashes and turbulence at the plasma edge. (a) The change in the magnetic field detected by the internal magnetic probe array for several crash cycles. (b) The fourier transform of the magnetic probe signals showing the mode structure of the turbulence. The crashes are associated with the m = 0 and m = 2 modes. (c) The plasma voltage for the times, showing the crash cycles. (d) The plasma voltage for the entire shot shown for reference, the time between the horizontal lines corresponds with the times shown in (a)-(c).

drop sharply. This confirms that the beginning of the voltage crash coincides with an expansion of the plasma toward the vessel wall, so it is plausible the the density gradient at the plasma edge changes rapidly during the crash, potentially allowing transient mode conversion of EBWs to X-mode radiation.

The emission spikes observed without the limiter display two characteristics of EBW emission. They correspond to frequencies around the second harmonic of the cyclotron frequency and the are polarized perpendicular to the magnetic field. In order to see if the emission depends on the density gradient, the local limiter was installed to modify this density gradient directly in front of the receiving horn.

We comment briefly on the radial emission in the frequency band between 30-40 GHz, which corresponds to the sixth harmonic of the cyclotron frequency at mid-plane. According to (3.29), a plasma with $n \sim 10^{20}$, $T_e \sim 90$eV in the MCX vacuum magnetic field will have an optical depth close to 800 at 35 GHz so we expect the EBW intensity in the overdense plasma to easily reach blackbody conditions. The UHR for the sixth harmonic will be at nearly the same radial location, but at roughly 6 times the density as the UHR for the second harmonic. For this higher density, assuming that the density gradient is roughly the same for the nearby UHR, (3.31) predicts a conversion efficiency of less than 1%. Radial emission measured in the range of 30-40 GHz using the Ka-band horn antenna indeed shows very weak emission. The receiver was scanned across the 30-40 GHz over the course of 40 discharges. Typical signals were just barely above the noise floor as shown in figure 6.12. The radial emission does not change significantly over this frequency range. Note that this measurement further supports the conclusion that refections do not

play a role in the emission measured at mid-plane, since the mirror throat plasma is in resonance with these frequencies and was shown with the axial measurements to generate significant ECE emission. If reflections from the transition regions could reach the radial horn antennas, then this radiation would be easily detected by the radial Ka-band horn.

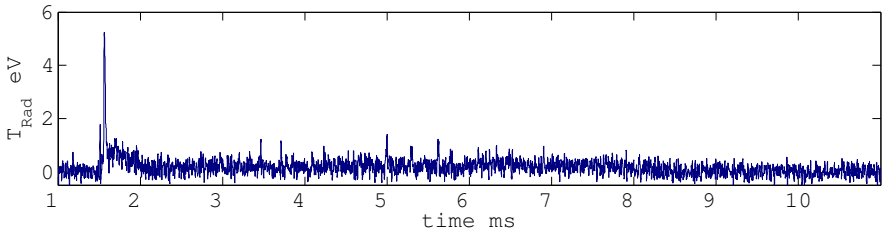

Figure 6.12 – X-modes emission looking radially at 33.0 GHz ($f = 6f_c$), emission is just above the noise floor.

6.5 Radial View with Limiter and Langmuir Probe Array

Because the design of the local limiter made it time consuming to alter the radial penetration of the limiter the limiter was installed in just four radial positions. First was the configuration without the limiter, corresponding to zero penetration by the limiter into the plasma, then with the limiter extending 0.5, 1.5 and 2.5 cm away from the vessel wall. The distance from the limiter to the rotating plasma could be altered for each configuration by slightly varying the magnetic mirror ration to move the LGFS closer to or farther away from the limiter. Representative results from each configuration are shown in Figure 6.13.

Clearly the placement of limiter can have a profound effect on the observed

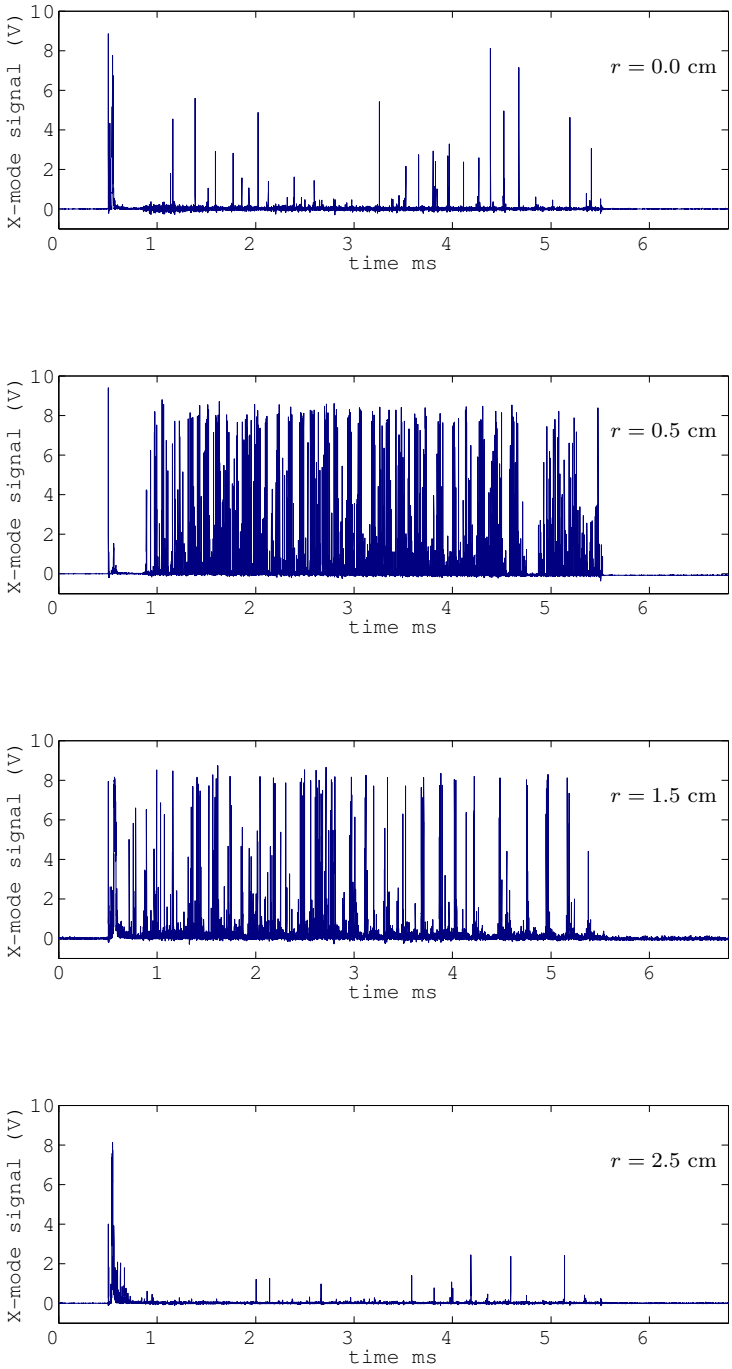

Figure 6.13 – Received X-mode emission for three different limiter configurations, first with no limiter and then with the limiter 0.5 and 2.5 cm past the LGFS. In all three shots the received is tuned to 11.5 GHz. $B_{mid} = .21$T, $M_r = 8.0$

emission characteristics. When the limiter is placed 0.5 cm from the rotating plasma edge the emission increases dramatically. The emission still consists of spikes, however the spikes are longer in duration, much more numerous and are clustered in bursts on the order of a hundred μs in length. These bursts, like the spikes in the limiterless case are strongly associated with plasma voltage crashes. When the limiter is extended 1.5 cm away from the wall the emission is intermediate between the two. Extending the limiter 2.5 away from the wall has the effect of shutting off the X-mode emission almost completely. In this configuration the limiter is extending out to the rotating edge of the plasma. This is an important observation, since there exists the possibility that the increased emission is the result of plasma-wall interactions with the limiter which may excite microwave emission near harmonics of the cyclotron frequency [13] and drown out any thermal signal. The fact that the emission is greatly reduced when the limiter is extended into the rotating plasma, where plasma wall interactions should be much greater lends confidence that the observed emission for the limiter at r = 0.5 cm is not being generated by the limiter-plasma interface. It is also worth noting that the limiter has been used both with and without the array of langmuir probes and that observed emission is the same for both of these cases. Furthermore, it is reasonable to expect that if the emission were generated by plasma-surface interactions at the limiter then the emission would be localized in frequency about twice the local cyclotron frequency at the edge of the limiter. The 2nd harmonic of the cyclotron frequency varies across the limiter owing to the inhomogeneous magnetic field between 10.56 and 10.70 GHz, while the observed emission ranges from 10.56 to more than 12.2 GHz, strongly suggesting

that the emission does not arise directly from plasma interactions with the limiter.

A question that must be answered immediately is whether or not the emission remains polarized, since the introduction of the limiter has obviously changed the emission properties of the plasma significantly. The microwave emission was measured in X-mode over the course of 48 discharges and the receiver frequency was varied shot to shot. The emission for each frequency was averaged from 2-4 ms after the initial breakdown, and this value was then averaged over three discharges. The orientation of the horn was then rotated to receive in the O-mode and the same measurements taken. The results are shown in figure 6.14. The average emission in the X-mode emission is as much as five times greater than the O-mode emission, showing that the limiter has no effect on the polarization of the radiation, again ruling out reflected ECE from the mirror throats as a possible source for the observed emission.

Assuming the emission bursts are driven by EBWs in the interior of the plasma, then the frequency spectrum will be dependent on the strength of the magnetic field, just as in the case of ordinary electron cyclotron emission. Large changes in the magnetic field simultaneously alters the plasma rotation, density and temperature [35], which can make direct comparisons between shots at different field strengths difficult. Relatively small changes in the field, on the order of 5%, should produce measurable changes in the emission spectrum without greatly altering the discharge characteristics. The frequency spectrum as a function of magnetic field was studied by running a series of discharges to accumulate emission spectra for mid-plane peak fields of 0.20T, 0.21T and 0.22T and the results are shown in figure 6.15. In all three

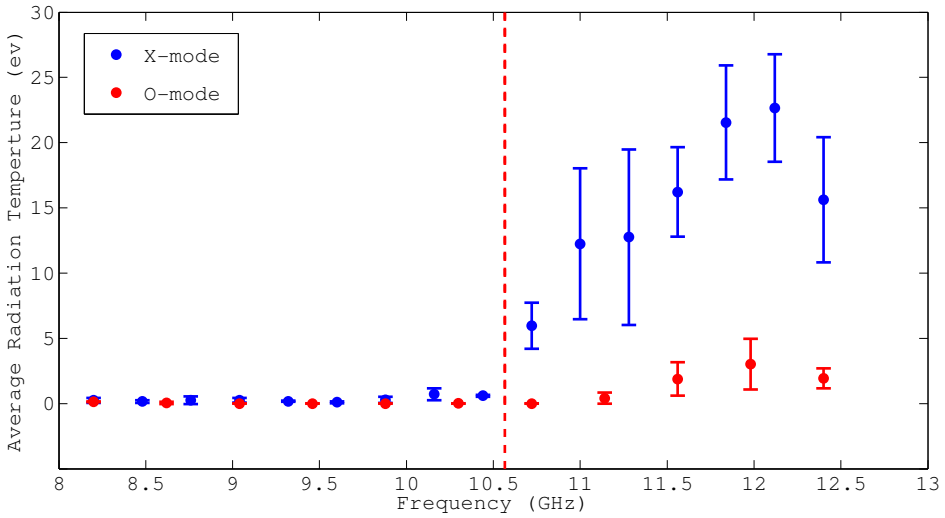

Figure 6.14 – Average radiation temperature measured radially in the X- and O-modes. The dashed red line corresponds to $f = 2f_c$ at the vacuum vessel wall. The disparity in the average intensities show that emission is strongly polarized in the X-mode.

cases emission is seen to occur only at frequencies for which $\omega = 2\omega_c$ is satisfied for some location in the plasma. In the case of $B_{mid} = 0.20$T, the emission falls to zero above about 12 GHz, a feature not seen in the spectra for higher fields. This is consistent with the EBW hypothesis: as the frequency increases, the region of the plasma in resonance with the wave recedes from mid-plane towards the mirror throats, eventually moving out of the horn's field of view.

If the emission bursts are caused by transient mode conversion of EBWs it is reasonable to assume that the timing between spikes would be related to the rotation velocity. Essentially, regions of favorable density gradient are swept around by the plasma rotation and periodically allow the trapped EBWs to escape to the receiving horn. This idea can be tested by measuring the distance between each emission spike and the next spike in the time series. This time difference can then be used to calculate a rotation speed assuming a radius of 0.27m and an m = 2 mode structure. The calculated velocity can then be compared to the rotation velocity measured by the internal ring of magnetic probes. The results of this analysis are shown in figure 6.16.

This technique has been used to estimate the rotation velocity of the emitting plasma across all observed frequencies. If the emission bursts were generated directly by the plasma with the corresponding cyclotron frequency, then the timing between spikes should correspond to the rotation speed in the middle of the rotating plasma. If instead, the emission bursts result from mode-converted EBWs then the timing between spikes should correspond to the motion at the UHR. For frequencies such that $\omega = 2\omega_c$ is satisfied somewhere in the plasma the results are in good agreement

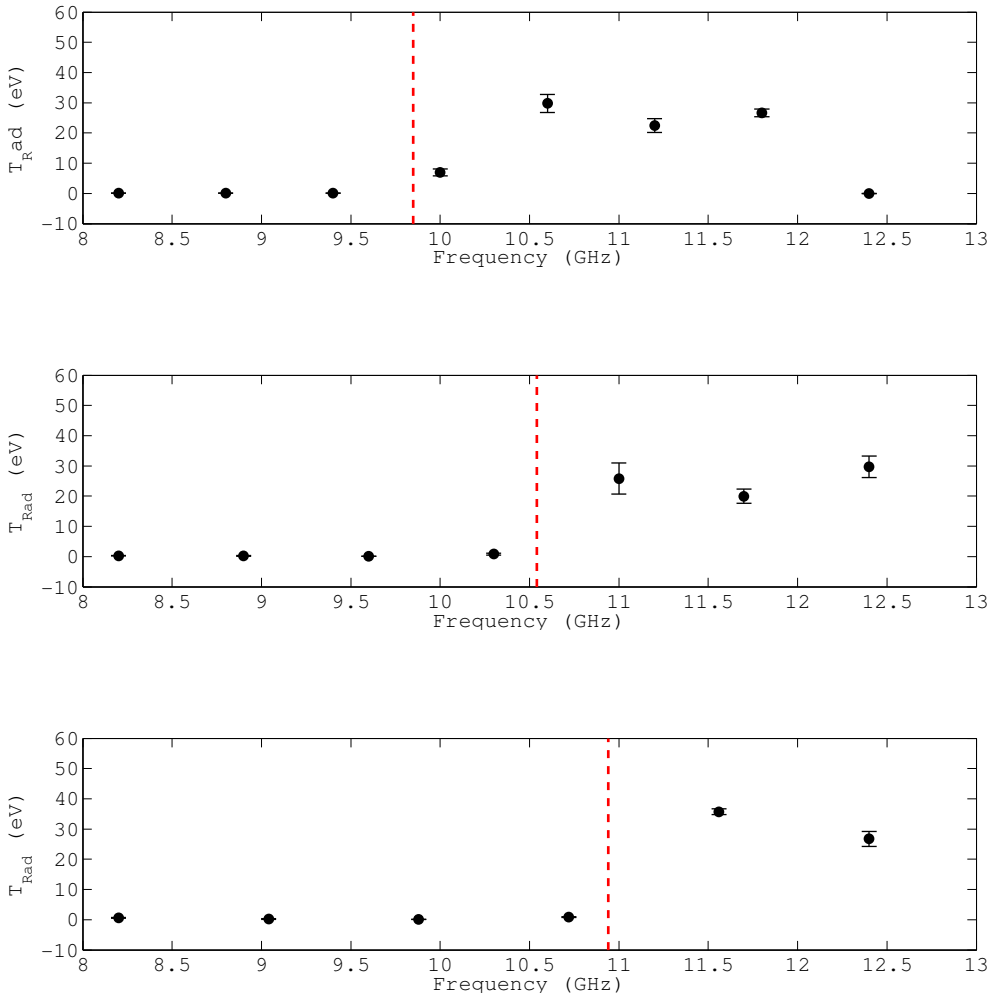

Figure 6.15 – Average radiation temperature spectrum for three different mid-plane field strengths. (a) $B_{mid} = 0.20$T, (b) $B_{mid} - 0.21$T, (c) $B_{mid} = 0.22$T. The dashed red lines indicates $f = f_{\omega_c}$ at the vacuum vessel wall for the different magnetic field strengths.

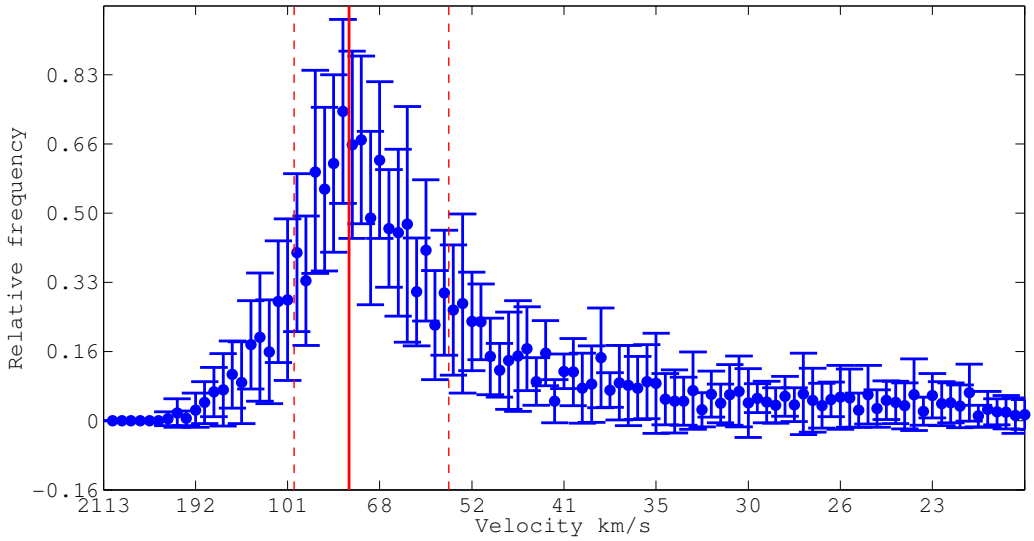

Figure 6.16 – Histogram of the average rotation velocities calculated using the spacing between bursts of X-mode emission at 11.0 Ghz. The solid red line indicates the average velocity measured by the internal magnetic probes assuming an m = 2 mode structure. The standard deviation in the mean velocity measured by magnetic probes is indicated by the dashed red lines.

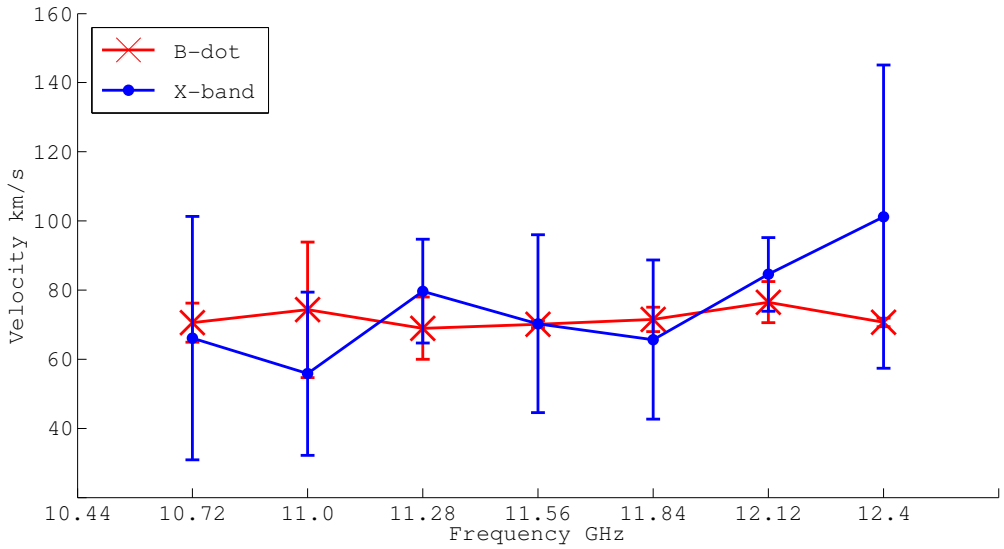

Figure 6.17 – Average edge rotation velocity calculated from the X-band data as a function of frequency. The average rotation velocities measured using the internal magnetic probes for the same discharges are shown for comparison.

with the internal magnetic probes. The results, for frequencies above ω_{cmin} are shown in figiure 6.17. These measurements demonstrate that regions of plasma generating the X-band emission at frequencies that correspond to the interior of the plasma are localized to the plasma edge and not the plasma interior which rotates at speeds between 100 and 150 km/s. [6]

Having established mode converted EBWs as the most likely mechanism for the emission bursts, the mode conversion efficiency is estimated using the array of electrostatic probes in front of the microwave horn. A difficulty that arises in measuring the density gradient is that the plasma edge rotates with a velocity around 70 km/s, so that the plasma viewed by the receiving horn is replaced every 3.5 μs, which is below the time response of the double probes. At best then, the probes

will give a rough indication of when conditions in front of the receiving horn are favorable to mode conversion. Figure 6.18 shows time traces for the received X-mode signal together with the density measured at the edge of the local limiter by the leading double probe. The bursts and spikes in the microwave signal are clearly related to the increased density at the edge of the limiter, supporting the case that the emission is related to the density in front of the receiving horn. The two signals shown in figure 6.18 are correlated at about 50 percent.

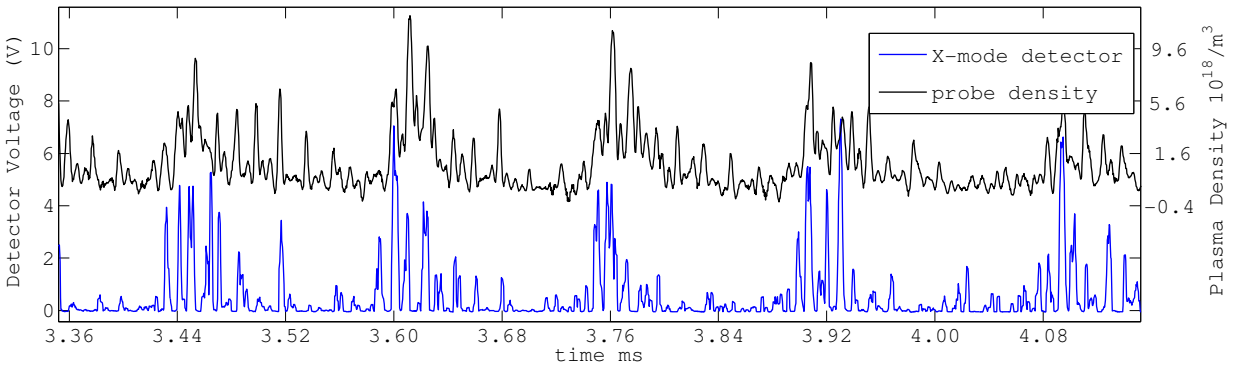

Figure 6.18 – Detected EBW signal at 12.0 GHz and plasma density measured by the leading double probe. Both signals have been filtered using a moving boxcar average with a window of 5 μs for clarity.

Data from all three probes is presented in figure 6.19 along with an estimation of L_n at the UHR. Calculating the density based on the double probes requires an estimation of the electron temperature at the probe tips. The tips of the probes are at the edge of the rotating plasma, where the electron temperature is likely to be reduced by interactions with neutral particles from the walls so the electrons are not expected to be more than a few eV at most. The radiation temperature measured

in the X-mode corresponding to plasma at the LGFS is between 1-5 eV, so this is the temperature range used in calculating the density gradient.

A significant source of error is that the density at the UHR will be on the order of $10^{18}/m^3$ while the probes record densities that are generally higher than this value indicating that the mode conversion layer is located just behind the probes. Two approaches have been attempted in order to overcome this limitation by estimating the density gradient behind the probes and calculate L_n. The first method is to assume that the density gradient is linear, and use the gradient measured by the three probes to calculate L_n using (3.34) with the absolute value of the density at the UHR given by $\omega_h^2 = \omega_p^2 + \omega_c^2$ which can easily be solved for n because the magnetic field directly in front of the horn is well known. The second approach is to assume the the density will decay roughly as an exponential inside the limiter. The average ratios of the densities measured by the three probes are fit to an exponential curve which is then used with the same density as before to calculate L_n. The two approaches can be compared by using the predicted density scale lengths to calculate the B-X conversion efficiency for real MCX discharges and comparing the predictions to the measured X-mode emission. This comparison is shown in figure 6.20. The exponential fit generates a result which is qualitatively similar to the observed emission, although the correlation between the two is only 44 percent. The linear fit, on the other hand, shows little resemblance to the observed signal, and the correlation with the observed signal is -23 percent. The exponential fit to the density measurements clearly gives a superior model and will be used in the interpretation of all further data.

While the predicted emission is poorly correlated with the observed emission, the qualitative agreement is sufficient to justify using the exponential estimation of L_n to calculate the average B-X conversion efficiency during the discharge and constrain the electron temperature in the interior of the plasma. In order to find the average conversion efficiency, a series of 27 discharges was taken under uniform experimental conditions. The density fluctuations in front of the receiving horn were measured using the array of double probes. These measurements were then used to calculate the B-X conversion efficiency as a function of time for each shot. Finally, the average B-X conversion efficiency for a "typical discharge" is computed and used to calculate the temperature of the electrons in the interior of the plasma. These measurements are shown in Figure 6.21 which shows both the average radiation temperature and electron temperature measured using the conversion efficiency of a "typical discharge." As discussed in chapter 5 the emission at a given frequency represents an average of the electron temperature over a region that spans a considerable radial section. The next section will use the numeric code describes in chapter 5 to address the question of the radial temperature profile.

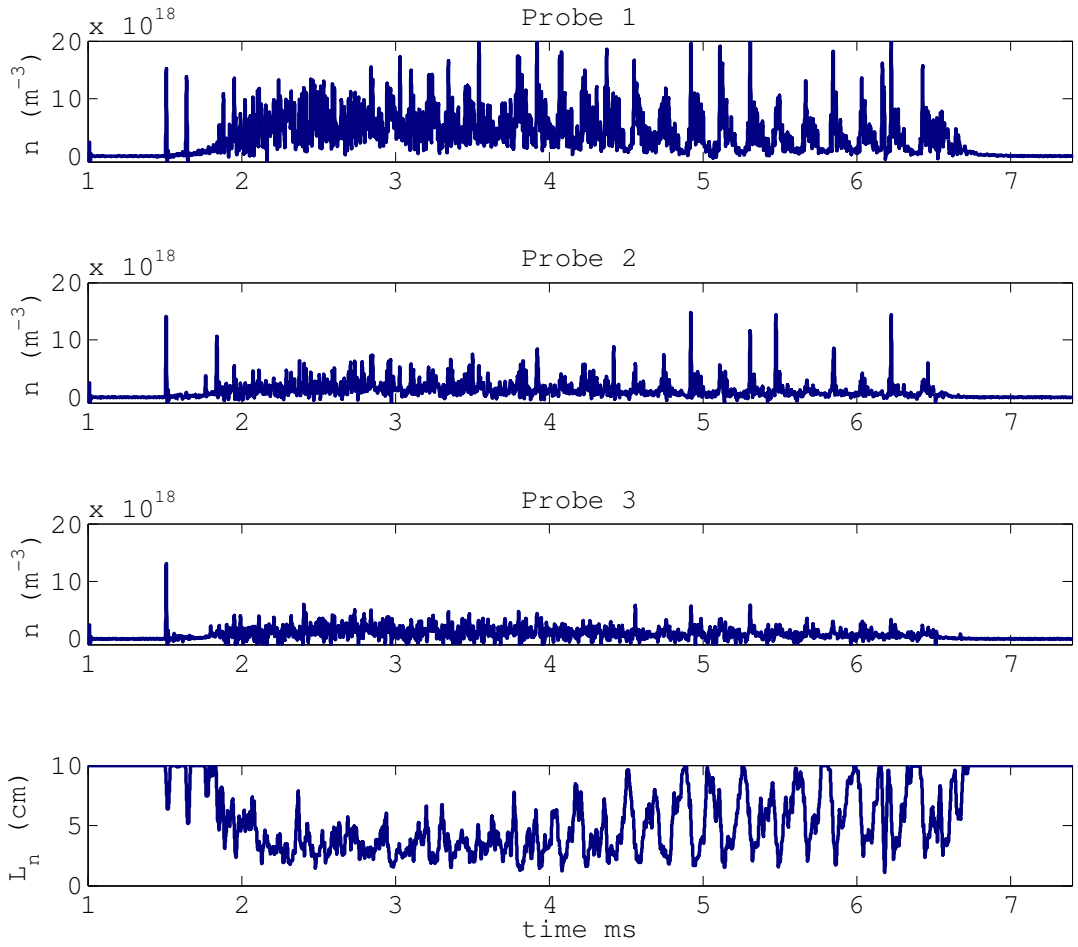

Figure 6.19 – Plasma density measured by the array of electrostatic double probes and the resulting calculation for L_n as a function of time.

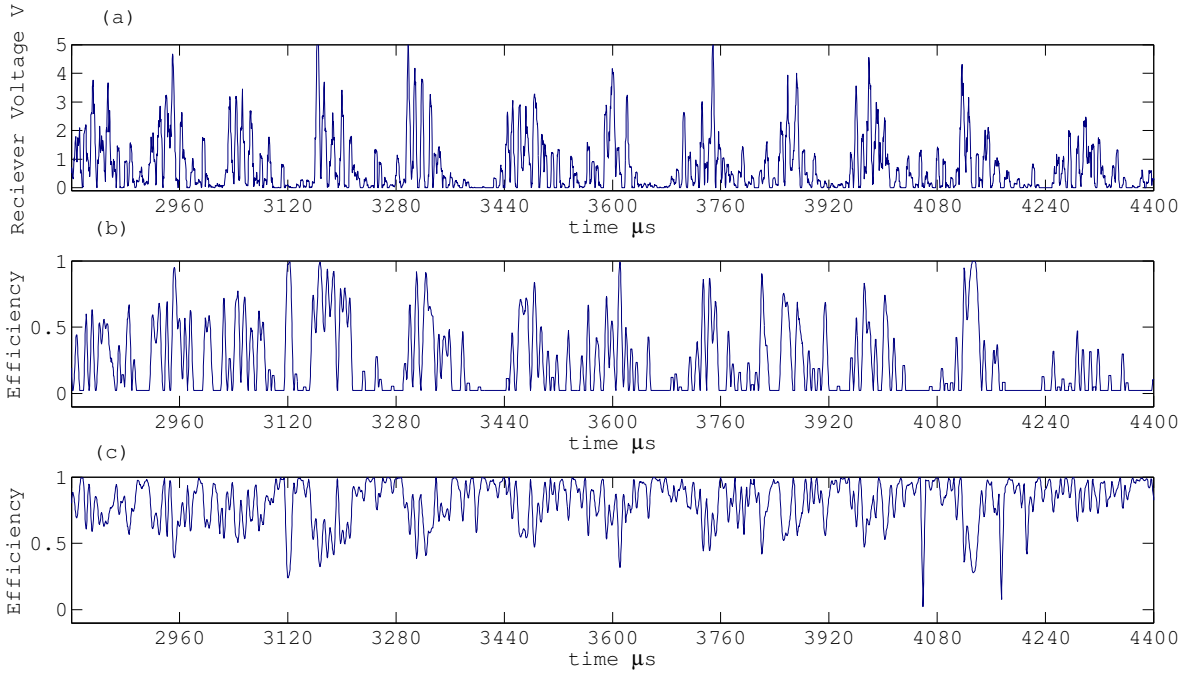

Figure 6.20 – Comparison of the linear and exponential estimates for L_n. (a) The received X-mode emission from a typical discharge measured at 11.56 GHz. (b) Predicted B-X coupling efficiency based of an exponential fit to the probe data. (c) B-X conversion efficiency based on a linear density fit.

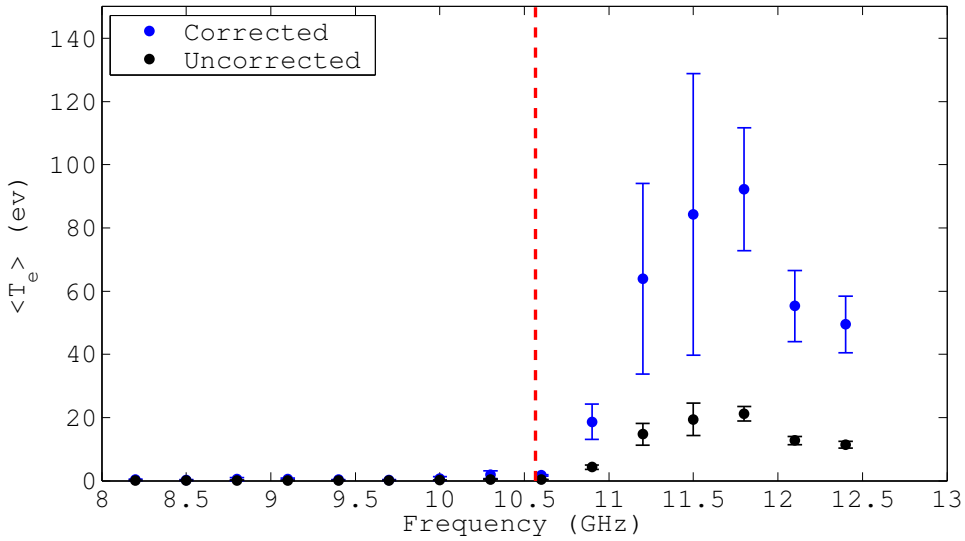

Figure 6.21 – Average electron temperatures as a function of frequency estimated from EBW emission. The first series (blue) is corrected for imperfect mode conversion using L_n calculated from the array of double probes. The second series (black) assumes perfect mode conversion. The dashed red line corresponds to $f = 2f_c$ at the vacuum vessel wall. Error bars for the corrected emission includes the uncertainty in the mode conversion efficiency as well as the standard deviation from the mean in the measured X-mode emission.

6.6 Electron temperature profile

In this section we compare the measured emission spectrum against theoretical predictions to estimate the electron temperature profile in MCX. Two magnetic field configurations were used to generate different spectra. The mirror ratio for each configuration was approximately 8 and the peak magnetic field at mid-plane was varied from 0.203 - 0.212T in order to change emission spectra. Emission spectra were collected by averaging the EBW emission at mid-plane from 1.5 - 2.0 ms after plasma breakdown and three shots were taken at each frequency. The measured spectra are compared to theory using the code described in chapter 5. The measured spectra are compared to the model in figure 6.22.

The code attempts to match the experimental values by calculating several possible emission spectra using using several possible values for the horn's effective viewing angle and the electron radial temperature profile. The horn's viewing angle is varied from 15-50 degrees in steps of 1 degree, and the skew parameter s from -5 5 in steps of 0.1. The electron radial temperature profile is assumed to be a skewed parabolic profile with $T_e = 0$ assumed at the LGFSs. The emission spectra is calculated for all combinations of angles and radial temperature profiles and the final fit determined by least squares minimization. The theory accurately predicts the emission at the low end of each spectrum, however it diverges at higher frequencies. One possible explanation for this is the simplistic nature of the code, which assumes that the horn's view is a perfect triangle.

For both of the spectra in figure 6.22, the code predicts an electron temperature

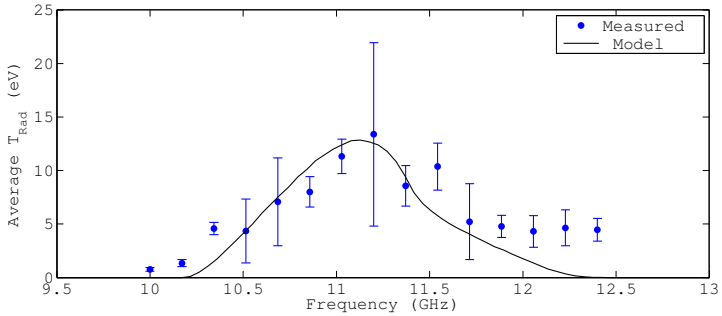

(a)

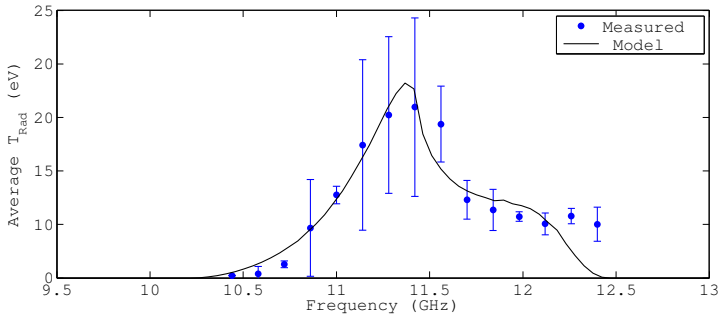

(b)

Figure 6.22 – Measured EBW emission spectra at mid-plane for B_{mid} = 0.194T (a) and $B_{mid} = 0.203$T (b)

skewed towards the core ($s = -1$) and horn angles of 39 (high field) and 41 (low field) degrees. The predicted electron temperature profile is shown in figure 6.23 together with the ion temperature profile measured using doppler spectroscopy. The electron temperature profile is in reasonable agreement with the ion temperature profile, although the electrons are generally somewhat colder than the ions with $Ti/Te \sim 1.5$.

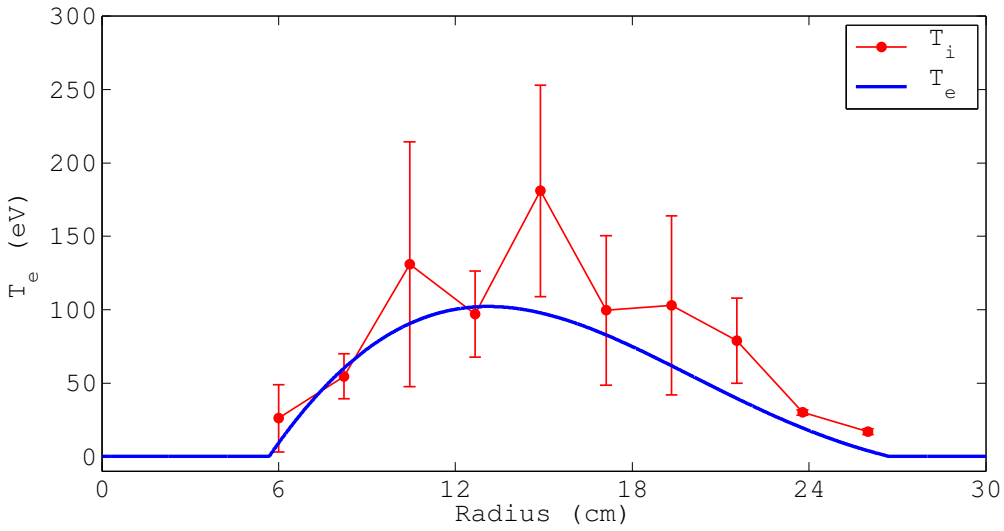

Figure 6.23 – The electron temperature profile which produces the best fit to the measured EBW spectrum. Shown with the ion temperature profile measured using doppler spectroscopy. [6]

6.7 Electron and ion equilibrium

The plasma in MCX is principally heated through viscous heating due to the extreme velocity shear in the plasma rotation, which primarily heats the ions. [36] Energy is then transferred to the electrons via collisions, and lost to electron

recycling at the insulators. Because the thermal speed for the electrons is much higher than for the ions, the electrons are not centrifugally confined and may readily collide with the insulators. By balancing the heat delivered to the electrons by collisions with the ions against the heat lost to recycling at the insulators we can estimate the equilibrium electron temperature.

The rate that energy is delivered to the individual electrons by the ions is estimated to occur on the time scale of the ion-electron collision frequency, modified by the mass ratio, and is proportional to the difference in temperatures between the ions and the electrons. [37] The total power is just this rate multiplied by the total number of electrons in the interior of the plasma. In terms of experimental parameters this gives us,

$$\frac{dT_e}{dt} = \nu_{ei} \frac{me}{mi} \left(T_i - T_e\right) n_e \pi \left(R_{ofs}^2 - R_{ifs}^2\right) L \tag{6.6}$$

here, L is the length of the mid-plane region, R_{ofs} and R_{ifs} are the radii of the inner and outermost rotating flux surfaces.

The heat lost by the electrons exiting along the field lines and being recycled at the insulators can be found with reasonable estimations of the electron density and temperature at the insulators. An upper limit on the energy lost to the insulators is found by assuming that all the electrons crossing a surface perpendicular to the magnetic field directly in front of the insulators are recycled. Setting the area of this surface equal to the annulus defined by the inner and outer rotating flux surfaces at the insulators, this gives

$$\frac{dT_e}{dt} = T_e n \frac{v_{th}}{2} \pi \left(R_{ofs}^2 - R_{ifs}^2 \right) \tag{6.7}$$

where the density, thermal velocity, R_{ofs} and R_ifs are evaluated at the insulators. This expression overestimates the heat loss by assuming hot electrons from the mid-plane of MCX make up fully half of the electrons in the plasma near the insulators, but offers a reasonable order of magnitude estimation for the end losses. The plasma at the insulators is not well diagnosed because the position of the insulators in the vacuum vessel and of the external mirror coils places the insulators well away from any access ports. For this calculation the density is estimated from MHD theory. In a centrifugally confined plasma the density along the field lines is expected to fall as, [3]

$$\rho \sim \rho_0 e^{-M\left(R_0^2 - R(z)^2\right)} \tag{6.8}$$

where $R\,(z)$ is the radius at a given z location and M is a parameter that depends on the sonic Mach number. The mach parameter M is fixed using the densities measured at mid-plane at the transition region by the interferometers. Once M is determined, the density at the insulators is calculated from the peak density measured at mid-plane. During the first millisecond of a typical discharge, the mid-plane density is greater than the transition region by a factor of 5-10, giving $M = 40 - 60$. For mid-plane densities around 5 x 10^{20} m^{-3} the corresponding insulator densities are around 1-3 x 10^{19} m^{-3}.

The most recent measurements of the ion temperatures [6] indicate tempera-

tures between 100 - 150 eV. Using these ion temperatures and equating (6.6) with (6.7) yields a predicted electron temperature between 87-128 eV in reasonable agreement with the EBW temperature measurement. The heat exhaust implied by the ratio of the measured ion to electron temperatures is 0.6 - 1.6 MW, indicating the electron recycling at the insulators may account for as much as 25% of the heat lost by the plasma.

Chapter 7

Conclusion

7.1 Summary

Microwave emission has been observed radially on MCX that is consistent with electron Bernstein emission with a radiation temperature of 20 eV. There is strong evidence that reflections have been successfully minimized and have do not impact of the received microwave emission. Failure to find any X-ray emission from the rotating plasma shows that measured emission does not result from superthermal electrons. The electron Bernstein wave is expected to easily reach blackbody emission levels in the MCX plasma. Thus, the emitted radiation places a lower bound on the electron temperature at 20 eV.

A ceramic limiter has been used to modify the density profile near the UHR layer and improve the B-X conversion efficiency, but failed to deliver steady-state mode conversion. The B-X conversion efficiency remains transient at is related to turbulence at the edge of the rotating plasma. An array of three electrostatic probes confirms the relation between the density gradient in front of the receiving horn and amplitude of the measured emission. The best estimation of the average B-X conversion efficiency, based on the array of probes, is $\sim 20\%$. The emission spectrum is used to predict the most likely electron temperature profile. The predicted temperature profile, combined with the calculated B-X conversion efficiency indicates

an average electron temperature of 80 eV with a peak temperature close to 100 eV. The ratio of the electron to ion temperatures, found by balancing collisional heating against recycling losses at the insulators indicates that electron recycling at the insulators accounts for roughly 1 MW, or 25% of the energy leaving the plasma.

Radiation in the whistler mode has been observed but is contaminated by signals consistent with mode-converted EBW emission from the transition region. The inclusion of microwave absorbing materials along the regions of the vacuum vessel deemed safe from plasma exposure did not eliminate this contamination and the whistler emission was abandoned as a temperature diagnostic.

7.2 Future Work

The keys to making a successful EBW temperature diagnostic are controlling and measuring the density gradient at the UHR. The array of electrostatic probes is not the ideal method for measuring the density gradient. Each point measured to build up the density gradient measurement requires two data channels that each require vacuum feedthroughs and digitizers and takes up space around the antenna horns. The probe tips also have a short lifetime before cumulative damage from the plasma makes their signals unreliable. Repeated melting changes the surface area of the collecting tips, and evaporated tungsten that is deposited on the insulating jackets can eventually make contact between the two probe tips, effectively shorting the plasma signal. The probe array used in these studies began to deteriorate after approximately 60 discharges, which is too short a life time to be a long term

diagnostic.

Microwave reflectometry could potentially be used to make rapid measurements of the density gradient. For this measurement, a wave is launched from the receiving horn with a frequency below the cutoff frequency of the plasma. The propagates to the plasma edge and is reflected off of the cutoff back to the antenna. The phase of the reflected wave is measured compared to the phase of the incident wave to infer the distance between the antenna and the cutoff. Sweeping the frequency of the emitted wave then allows for a relatively fast measurement ($\sim 10\mu s$) of the density gradient. The measurement of the density gradient can be done using the same horn used for the EBW measurements. First the density gradient is measured, then a fast ferrite switch could be used to switch the antenna into the radiometer. Alternating measurements of the density gradient and EBW emission give the time history of the electron temperature. The limitation for this technique is the time needed to measure the density gradient. From chapter 6 we know that the plasma gradient in front of the X-band horn changes dramatically on a timescale around 10 μs, so that the density gradient just recorded may no longer apply during the EBW recording.

One possible resolution to this issue would be to move the UHR further away from the rotating flux surface, so that the density perturbations caused by the turbulence would have less impact on the UHR. In a larger device where the LGFS could be several centimeters removed from the walls this would be relatively simple. The increased distance between the rotating plasma and the chamber walls would allow for a smoother density gradient and place the UHR further from the turbulent

edge. On MCX the problem is more difficult, as the plasma density would have to be artificially extended past radial position of the main chamber wall and into the recession containing the antenna.

The codes used to analyze the EBW emission employ fairly crude models. Much more precise information could be obtained with the use of a ray-tracing code such as, GENRAY which solves the full warm plasma dielectric tensor in order to calculate EBW propagation and damping. A full wave code to calculate the B-X mode conversion efficiency would also greatly improve the precision of the temperature measurements. The codes are freely available and have been used on larger experiments with overdense plasmas such as, MAST, MST, NSTX. [25], [26], [38] With these tools it would be possible to better predict where in the plasma the EBWs are generated, and how effectively they couple to the X-mode in order to build up a more accurate temperature profile.

While the whistler wave is not useful as a temperature diagnostic on MCX, it may prove useful on a larger scale centrifugal experiment. The chief obstacles are the EBW contamination and passage of the signal through the insulator. Reflection are less of a challenge in a large device because the characteristic length scales of the machine are much larger compared to the wavelength of the emission, allowing the beam to be focused on a relatively small section of the machine.

In light of the fact that 25% of the energy leaving the plasma is likely lost to the insulators by the electron recycling, it is clear that a focus of any work advancing the centrifugal confinement scheme must be reducing the electron flux to the insulators. As shown by (6.7) and (6.8), the heat lost via recycling at the

insulators depends on the surface area of the plasma-insulator interface and the electron density and temperature at the insulators. One approach to reduce the heat loss is to increase the mirror ratio, essentially narrowing the nozzle through which the electrons need to pass. A potential drawback is that this approach requires either increasing the magnetic field in the mirror throats, which requires more expensive magnets or reducing the field at mid-plane which implies a higher ratio of plasma pressure to magnetic pressure and invites instabilities. A second approach is to reduce the density at the insulators by increasing the sonic mach number. As the ion axial confinement improves at higher mach number and the density at the magnetic maximum falls, the electron density and therefore electron recycling will also fall.

Another reasonable question to address is where does the other 75% of the energy go? Electron recycling away from the insulators, at the metallic vessel wall is a possibility. Radiative recombination at the edge of the plasma, and radiation by impurity ions in the plasma are also likely candidates. The question could be addressed with the use of a bolometer to measure the radiative power emitted by the plasma in the visible and UV parts of the spectrum.

Appendix A

Electrostatic Probes

Electrostatic probes, commonly referred to as Langmuir probes, are a widely used to measure conditions in mild plasmas. The most basic probe consists of an insulated wire inserted into the plasma such that only the tip of the wire is exposed to the plasma. The tip of the probe is bombarded by electrons and ions from the plasma which may result in a net current in the wire. When connected to an appropriate circuit this current can be analyzed to calculate the plasma density, floating potential and electron temperture. [39] Obviously the utility of electrostatic probes is limited to use in plasmas cool enough for the probe to survive the heat flux from the plasma.

The current drawn by the probe depends primarily on the potential of the probe relative to the surrounding plasma. When the probe tip is isolated from ground so that very little current is drawn by the probe, then the larger flux of electrons will rapidly build up negative charge on the probe until a sufficient electric field develops to deflect the majority of incoming electrons and balance ion and electron flux. The probe is then said to be at the floating potential; note that this is different from the electric potential of the plasma. If the probe tip is biased sufficiently negative relative to the surrounding plasma then the impinging electrons are reflected and current is equal to the ion flux. This current is nearly independent

of the biasing voltage and is called the ion saturation current. In the opposite case the probe may be biased positive to the surrounding plasma, repelling the ions and the probe is said to be drawing electron saturation current.

In almost all plasmas, the ions will have a slower thermal velocity than the electrons, so that drawing ion saturation current results less heat being delivered to the probe than drawing electron saturation current. For this reason probes are often biased negative with respect to the plasma potential so as to avoid collecting electrons and reducing potential damage to the probes. A further advantage of using ion current is that the smaller current is less perturbing to the surrounding plasma.

If the ion and electron temperatures are known then the ion saturation current density is given by, [39].

$$j_{0i} = \begin{cases} \frac{1}{4} ne \sqrt{\frac{8kT_e}{\pi m_i}} & : (T_i \leq T_e) \\ \frac{1}{4} ne \sqrt{\frac{8kT_i}{\pi m_i}} & : (T_i \geq T_e) \end{cases} \tag{A.1}$$

In MCX the ions are generally expected to be hotter than the electrons so the second condition is used when interpreting the results from the array of double probes. Three important questions have to be answered in the course of interpreting data from Langmuir probes in MCX. The possible of collisional effects, which may limit the ion flux to the probe as the ions must diffuse toward the probe surface. The magnetic field limits the motion of the ions and electrons to different degrees, with the ion Larmour radius being much larger than for the electrons. Thus the magnetic field may asymmetrically alter the ion and electron collisions with the probe. Finally, rapid fluctuations in the floating potential of the plasma introduce

signals which are difficult to distinguish from changes in the density. The relative importance of the first two effects depend on the typical size scale of the probe, a. For the double probes used in measuring the density grad ient $a \sim 0.1$ cm. If the plasma is highly collisional then the ions will have to diffuse from the bulk plasma to the probe rather than being drawn freely to the biased probe. The plasma in the vicinity of the probe can be considered collisionless when the mean free path is much larger than the typical dimensions of the probe. Otherwise the current delivered to the probe is reduced by roughly the ratio of the mean free path to the probe radius. If the mean free path for the ions is given by $\lambda_{mfp} \sim v_{th}\nu_{ii}$, for the conditions near the LGFS ($n = 10^{19}m^{-3}$ $T_i \sim 10$ eV), $\lambda_{mfp} \sim 1\text{cm} \gg a$ so the affects of collisions of the ion saturation current may be safely neglected.

The magnetic field alters the dynamics of the particles near the probe tip, limiting the motion of the particles across the magnetic field. As long as the ion gyroradius is much greater than the probe dimensions, (A.1) may be used to evaluate the ion saturation current. [12] At the mid-plane the ion gryoradius is $\rho = m_i v_{th}/eB \sim 1.6$ cm $\gg a$, it is justifiable to ignore the magnetic field's affect on the ion saturation current. Dynamic floating potentials pose a more serious concern for density measurements in MCX, because rapid changes in the floating potential can induce currents in the probe which cannot be distinguished from the currents due to density. There are two common approaches to dealing with dynamic floating potentials. The is to increase the biasing voltage V_0 until it is much larger than the rage of the floating potential, but floating potentials at the MCX mid-plane can exceed several hundred volts, making this approach unappealing. The second ap-

proach, and the one used for this work, is to employ a double probe. In this scheme, two metallic probes are placed near each other in the plasma and both are isolated from ground. If one probe is then electrically biased against the other a current will flow between the probes while no net current is drawn so that both probe tips float near the plasma floating potential. If the biasing voltage is such that $V_0 \gg kT/e$ then the current drawn is equal to the ion saturation current. A circuit suitable for measuring the plasma density with a double probe is shown in figure A.1. There are a few considerations in the design of the circuit. The biasing voltage must be large enough that $V_0 \gg kT_e/e$ to ensure that the probe is biased to saturation. The resistors should be chosen such that $R \gg R'$ and $I_s/R' \ll V_0$ to ensure that both probes remain near the floating potential and that the biased probe remains at V_0 relative to the unbiased probe. The isolation transformers are critical in pulsed experiments such as MCX in order to avoid ground currents as the vacuum vessel potential may rise several volts above instrument ground, overwhelming the probe signals and potentially damaging fragile digitizers.

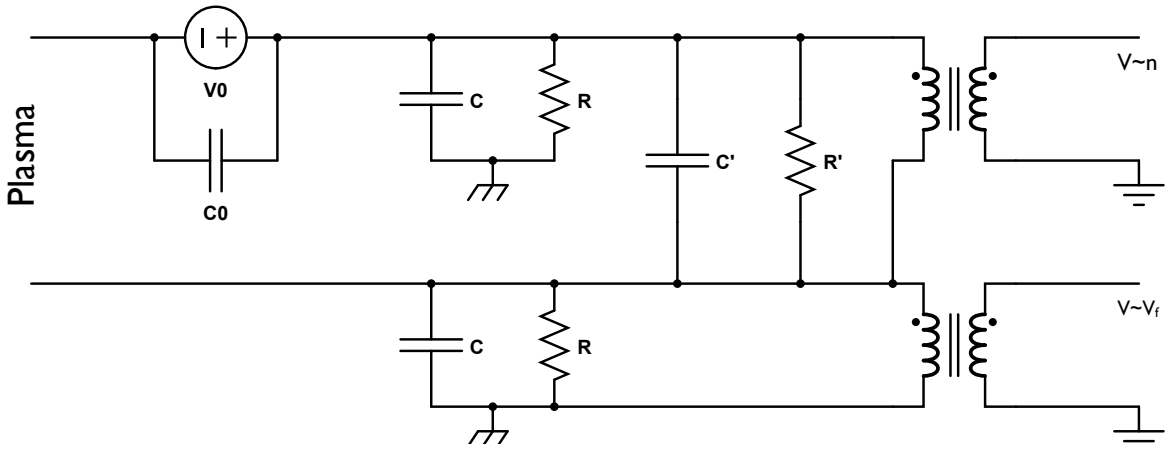

Figure A.1 – Circuit suitable for measuring the plasma density and floating potential using a double probe.

Bibliography

[1] R.F.Ellis, A. Case, R.Elton, J. Gosh, H. Griem, A. Hassam, R. Lunsford, S. Messer, and C. Teodorescu. Steady supersonically rotating plasmas in the maryland centrifugal experiment. *Physics of Plasmas*, 12:055704 1–7, 2004.

[2] Yi-Min Huang and A.B. Hassam. Velocity shear stabilization of centrifugally confined plasma. *Physical Review Letters*, 87:235002 1–4, 2001.

[3] A. B. Hassam. Steady-state centrifugally confines plasmas for fusion. *Comment Plasma Physics and Controlled Fusion*, 18:263–279, 1997.

[4] C. Teodorescu, R.F. Ellis, A. Case, C. Cothran, A. Hassam, R. Lunsford, and S. Messer. Experimental verification of the dielectric constant of a magnetized rotating plasma. *Physics of Plasmas*, 12:062106–1–6, 2005.

[5] J. Gosh, R.C. Elton, H.R Griem, A. Case, R. Ellis, A. B. Hassam, S. Messer, and C. Teodorescu. Spectroscopic measurements of plasma rotation and ion and neutral atom temperatures in the maryland centrifugal experiment. *Physics of Plasmas*, 12:062106–1–6, 2005.

[6] C. A. Romero-Talamás, R. C. Elton, W.C. Young, R. Reid, and R. F. Ellis. Isorotation and differential rotation in a magnetic mirror with imposed exb rotation. *Physics of Plasmas*, 19:072501 1–5, 2012.

[7] I. U. Uzun-Kaymak, P. N. Guzdar, S. Choi, M. R. Clary, R. F. Ellis, A. B. Hassam, and C. Teodorescu. Nonlinear mode coupling and sheared flow in a rotating plasma. *EPL*, 85:15001 p1 – p5, 2009.

[8] S. Choi, P. N. Guzdar, A. Case, R. Ellis, A. B. Hassam, R Lunsford, C. Teodorescu, and I. Uzun-Kaymak. Observations and analysis of magnetic fluctuations in the maryland centrifugal experiment. *Physics of Plasmas*, 15:042507 1 – 10, 2008.

[9] P. N. Guzdar, I. Uzun-Kaymak, A. B. Hassam, C. Teodorescu, R.F. Ellis, R. Clary, C. Romero-Talamás, and W. Young. Low dimensional model for the fluctuations observed in the maryland centrifugal experiment. *International Symposium on Waves, Coherent Structures, and Turbulence in Plasmas*, 1:148–157, 2010.

[10] B. Lehnert. Spectroscopic measurements of plasma rotation and ion and neutral atom temperatures in the maryland centrifugal experiment. *Nuclear Fusion*, 11:485–533, 1971.

[11] W. C. Young, A.B. Hassam, C.A. Romero-Talamás, R.F.Ellis, and C. Teodorescu. Diamagnetism of rotating plasma. *Physics of Plasmas*, 18:112505 1–3, 2011.

[12] I. H. Hutchinson. *Principles of Plasma Diagnostics*. Cambridge University Press, Cambridge CB2 2RU, UK, 2002.

[13] George Bekefi. *Radiation Processes in Plasmas*. John Whiley and Sons, inc, New York, 1966.

[14] M. A Heald and C. B. Wharton. *Plasma Diagnostics with Microwaves*. John Whiley and Sons, inc, New York, 1965.

[15] R. F. Ellis, G. D. Tsakirsis, and D. A. Boyd. Whistler-mode electron cyclotron emission in a mirror plasma. *Phys. Rev. Lett.*, 48:93–96, 1981.

[16] R. F. Ellis, G. D. Tsakirsis, and D. A. Boyd. Emission, absorption, and tunneling of whistler waves in an inhomogeneous magnetic field. *Physics of Fluids*, 26:1528–1544, 1981.

[17] R. F. Ellis, R. A. James, and C. J. Lasnier. Electron cyclotron emission diagnostics for mirror devices. *Review of Scientific Instruments*, 56:891–895, 1984.

[18] C. J. Lasnier, R. F. Ellis, G. D. Tsakirsis, R. A. James, and T. A. Casper. Whistler mode electron cyclotron emission from energetic electrons in tmx-upgrade. *Plasma Physics and Controlled Fusion*, 30:491–513, 1987.

[19] Thomas Howard Stix. *Waves in Plasmas*. Springer, New York, 1995.

[20] Heinrich Peter Laqua. Electron Bernstein wave heating and diagnostic. *Plasma Physics and Controlled Fusion*, 49:R1 – R42, 2007.

[21] M. Bornatici, C Maroli, and V. Petrillo. Electron cyclotron bernstein waves for quasi-perpendicular and oblique popagation. In *Heating in Toroidal Plasmas: Proceedings of the 3rd Joint Varenna-Grenoble International Symposium, Volume II.*, 1982.

[22] A. K. Ram and S. D. Schultz. Excitation, propagation, and damping of electron bernstein waves in tokamaks. *Physics of Plasmas*, 7(10):4084–4094, 2000.

[23] A. K. Ram, A. Bers, S. D. Schultz, and V. Fuchs. Mode conversion of fast Alfvén waves at the ion-ion hybrid resonance. *Physics of Plasmas*, 3(5):1976–1982, 1996.

[24] V. Fuchs, A. K. Ram, S.D. Schultz, A. Bers, and C.N. Lashmore-Davies. Mode conversion of and electron damping of the fast Alfvén wave in a tokamak at the ion-ion hybrid frequency. *Physics of Plasmas*, 2(5):11637–11647, 1995.

[25] Brent Manley Jones. *Electron Bernstein Wave Thermal Emission and Mode Conversion in the CDX-U Spherical Torus*. PhD thesis, Princeton, 2002.

[26] H.P. Laqua and H.J. Hartfub and W7-AS Team. Electron bernstein wave emission from and overdense plasma at the w7-as stellarator. *Phys Rev. Lett.*, 81(10):2060–2063, 1998.

[27] J. D. Jackson. *Classical Electrodynamics*. John Whiley and Sons, inc, New York, 1999.

[28] C. L. Olsein. Spatial electron cyclotron damping. *Physics of Fluids*, 16:160–165, 1971.

[29] R.F. Ellis, G.D. Tsakirsis, C.Z. Wang, and D.A. Boyd. Upper hybrid emission from a magnetized gas discharge plasma. *Plasma Physics and Controlled Fusion*, 28:327–345, 1985.

[30] J. D. Hubba. *NRL Plasma Formulary*. Office of Naval Research, Washington, DC 20735, 2009.

[31] G. Landaur. Generation of harmonics of the electron-gryrofrquency in a penning discharge. *Physics of Plasmas*, 4:395–400, 1962.

[32] H. Dreicer. *Plasma Waves in Space and in the Labratory*. University press, Edinburgh, 1969.

[33] F.W. Crawford, G.S. Kino, and H.H. Weiss. Excitation of cyclotron harmonic resonances in a mercury-vapor discharge. *Phys. Rev. Lett.*, 13:229–232, 1964.

[34] T. H. Stix. Radiation and absorption via mode conversion in an inhomogeneous collision-free plasma. *Phys. Rev. Lett.*, 15:878–882, 1965.

[35] Robert Lunsford. *Parametric Limitations on Discharge Performance in the Maryland Centrifugal Experiment*. PhD thesis, University of Maryland, 2007.

[36] B.R.Osborn, R.F.Ellis, and A.B. Hassam. Numerical simulation of the equilibrium and transport of a centrifugally confined plasma. *Physics of Plasmas*, 10:2389–2398, 2003.

[37] R.J. Goldston and P.H. Rutherford. *Introduction to Plasma Physics*. Taylor and Francis, 270 Madison Avenue, New York, NY 10016, 1995.

[38] P.K. Chattopadhyay, J.K. Anderson, T.M Biewer, D. Craig., and C.B. Forest. Electron bernstein wave emission from an overdense reversed field pinch plasma. *Physics of Plasmas*, 9:752–755, 2001.

[39] J.C. Sprott. Electrostatic probe techniques. Technical report, University of Wisconsin, 1966.